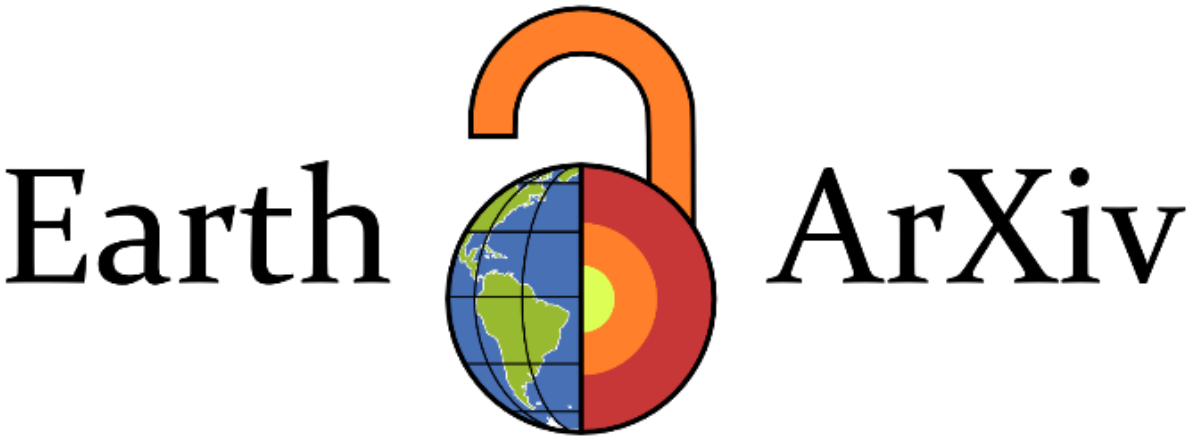

Time domain full waveform inversion with decomposed Gauss-Newton Hessian

Gaoshan Guo [1] *and Stéphane Operto* [1]

ABSTRACT

Full waveform inversion (FWI), a nonlinear data fitting approach for parameter estimation, is generally implemented with local optimization methods. The convergence of the iterations can be slow when the steepest descent direction provided by the negative gradient of the data misfit function is not preconditioned by the inverse full Newton Hessian or its linear approximation, namely the Gauss-Newton (GN) Hessian. Here, we present a novel generalized (or weighted) form of time-domain FWI allowing for a robust and computationally-efficient implementation of Gauss-Newton FWI. This weighted form of FWI is inspired by the extended-source formulation of FWI. In this framework, the GN Hessian of FWI can be decomposed into a source-side diagonal pseudo-Hessian in the model domain and a receiver-side Hessian in the data domain. The pseudo-Hessian corresponds to the auto-correlation of the so-called virtual sources, which is classically used to precondition the descent direction of FWI by scaling the amplitudes of the gradient. The receiver-side data-domain Hessian represents the Hessian of an underdetermined source problem. This source problem aims at estimating the volume scattering sources that would be generated by the interaction of the true incident wavefields with the unknown perturbation model at the current FWI iteration. The so-called adjoint fields of FWI are the adjoint approximations of these scattering sources. The pseudo-Hessian does not generate computational overhead, while the inverse data-domain Hessian is approximated by a multi-dimensional non-stationary matching filter for each source. Finally, the computational cost of one decomposed GN descent direction is two times that of the steepest descent. Numerical tests validate that the decomposed GN Hessian provides a reliable approximation of the GN Hessian. Alternatively, the weighted gradient by the inverse data-domain Hessian can be used in quasi-Newton methods with the diagonal pseudo-Hessian as preconditioner. Synthetic tests show that the decomposed GN Hessian not only accelerates the convergence of classical FWI but can also reconstruct more accurate velocity models when the initial model is not accurate.

INTRODUCTION

Over recent decades, full waveform inversion (FWI) has emerged as a cornerstone technique for characterizing subsurface structures with wavelength-scale resolution in the realm of oil and gas seismic exploration (Sirgue et al., 2010; Plessix and Perkins, 2010; Baeten et al., 2013; Warner et al., 2013; Operto et al., 2015; Métivier et al., 2024). Given the size of the data and model spaces, FWI classically employs gradient-based local optimization to iteratively refine model parameters by minimizing the least-squares (LS) data misfit function (Pratt et al., 1998), the gradient of which is efficiently computed with the adjoint-state

method (Plessix, 2006). The most basic local optimization method is the steepest descent (SD) method where the model is updated using the first derivative information. This method yields updates with unbalanced amplitudes in particular for surface-to-surface acquisitions because the gradient does not have the units of the model parameters. Thus, it must be deconvolved from experimental factors and wave propagation effects by amplitude scaling and non-stationary filtering. In SD methods, these effects are crudely accounted for through a step length estimated with a line search method (Nocedal and Wright, 2006), resulting in slow convergence of the optimization and potentially suboptimal models. More precise approaches involve the full Newton (FN) Hessian, which represents the second derivative information. The FN Hessian contains a linear term referred to as the Gauss-Newton (GN) or approximate Hessian, and a nonlinear term correcting the gradient for double-scattering effects (Pratt et al., 1998). The GN Hessian is formed by the inner product of the partial derivative data, which represent the recording at receivers of the scattered incident wavefields by virtual impulse sources sampling the subsurface with a given radiation pattern. The diagonal terms of the GN Hessian contain the squared amplitudes of the partial derivative data that are used to scale the gradient for geometrical spreading effects while the off-diagonal terms represent the band-pass filter generated by the limited bandwidth of the source and the limited spread of the acquisition geometry. Applying the inverse Hessian to the gradient mitigates these filtering effects by multidimensional deconvolution. Moreover, the Hessian mitigates the detrimental effects of parameter cross-talks in multiparameter FWI (Operto et al., 2013; Pan et al., 2016).

Despite the importance of Hessian in FWI, the explicit computation, storage, and inversion of the FN/GN Hessian remains impossible for realistic applications. Hence, different approaches have been developed to account for approximately the Hessian at a reasonable cost. In frequency-domain FWI, the truncated Newton method solves the normal equation associated with the Newton descent direction with few iterations of a conjugate gradient (CG) solver where the Hessian-vector product is computed with the second-order adjoint state method (Métivier et al., 2013; Pan et al., 2017; Gao et al., 2023). However, this approach is more complicated to implement in the time domain due to the management of the sources of the second-order adjoint-state equations (Yang et al., 2018; Yong et al., 2022). Quasi-Newton methods are also widely used to approximate the inverse of the FN Hessian from a few gradients of the previous iterations (Nocedal, 1980), such as the limited-memory BFGS (Broyden–Fletcher–Goldfarb–Shanno) (l-BFGS) (Brossier et al., 2009; Liu et al., 2021) and Anderson acceleration (Yang, 2021; Aghazade et al., 2022) methods. The drawback of these methods is that the FN Hessian is poorly approximated during the first iterations. When the data residuals are small, the second-order term in the FN Hessian is ignored, and the GN Hessian is a pertinent approximation. Hence, many developments focus on good approximations of GN iterations. The most basic approaches consider the diagonal terms of the GN Hessian to scale the amplitudes of the FWI gradient (Ravaut et al., 2004; Operto et al., 2006). Alternatively, Shin et al. (2001) proposes an approximate or pseudo diagonal Hessian by replacing the partial derivative data by their virtual sources in the expression of the diagonal coefficients. Unlike the exact diagonal Hessian, the pseudo-Hessian can be computed on the fly at the same time as the gradient without computational overhead. These diagonal approximations can be used as a preconditioner for quasi-Newton or Truncated Newton methods (e.g. Métivier and Brossier, 2016). However, it overestimates the subsurface illumination, resulting in the wrong resolution function (Tang and Lee, 2010; Liu et al., 2022).

More advanced methods have been proposed to better approximate the GN Hessian in the framework of LS ray-based and wave equation-based migrations. These methods may be adapted for FWI since the gradients of LS migration and FWI rely both on the adjoint of the Born modeling operator keeping however in mind that FWI doesn't rely on the high-frequency (asymptotic) approximation. Jin et al. (1992); Lambaré et al. (1992); Thierry et al. (1999b,a) recast the ray-based inverse scattering problem, originally formulated by Beylkin (1985) as the direct inversion of a generalized (weighted) Radon transform, in the framework of LS inverse theory. In this ray-Born approach, the scattered data misfit function is weighted by a parameter-dependent operator such that the model-domain GN Hessian becomes a band-limited Dirac function, implemented approximately as a scaled identity function (Lambaré et al., 2003). Most of the amplitudes and illumination effects are taken into account in the gradient by weighting the scattered data by several ray quantities involving amplitudes and illumination angles. Rickett (2003) and Guitton (2004) approximate the effects of the inverse Hessian in wave-equation migration with an image-to-image fitting approach. Rickett (2003) performs a pointwise division between the migrated section and its demigrated/remigrated version, while Guitton (2004) approximates the inverse Hessian by matching filters. Alternatively, Khalil et al. (2016); Liu and Peter (2018) implement this matching-filter approach in the data domain with stationary Wiener filter. The computational cost of the data-domain approach is two times that of LS ray-Born migration. Khalil et al. (2016) show that the data-domain implementation leads to a better-migrated image in under-illuminated areas involving steeper reflectors. Symes (2008) recasts the image-to-image fitting approach of Rickett (2003) and Guitton (2004) in the framework of asymptotic ray theory and exploits the mathematical properties of pseudo-differential operators to implement the inverse of the Born modeling operator as a scaling and Laplace filtering of the migrated section. Furthermore, ten Kroode (2012); Hou and Symes (2015, 2017); Chauris and Cocher (2017) approximate the inverse of the extended Born modeling operator for Kirchhoff or ray-Born linearized waveform inversion. The kernel of the extended Born modeling operator involves unphysical subsurface offsets that extend the search space of the velocity model building problem. In these approaches, the approximate inverse of the extended Born modeling operator can be decomposed into easy-to-compute model-domain and data-domain weighting operators applied to the adjoint of the extended Born modeling operator (Hou and Symes, 2015, their equations 1, 24, 28). The computation of the weighting operators doesn't generate significant computational overheads and doesn't involve any ray-based quantities. Finally, Hou and Symes (2016) adapt this formulation to approximate the GN iteration for FWI by removing the footprint of the extended space (i.e., by considering only the zero subsurface offset) in the model-domain weighting operator.

In this study, we propose a new implementation of GN iterations for FWI, which finds its roots in the extended-source (ES) formulation of FWI (Gholami et al., 2022; Operto et al., 2023; Guo et al., 2024). ES-FWI extends the linear regime of FWI by computing wavefields that fit the data without cycle skipping. These extended wavefields are the sum of the FWI background wavefields and an approximation of the scattered wavefields by the sought model perturbation at the current FWI iteration. These scattered wavefields are unknown. However, their restriction on the receivers, namely the data residuals, are known. Therefore, the best we can do to approximate the true wavefields is to first estimate the sources of the scattered wavefields by fitting the FWI data residuals in the LS sense and then compute wavefields with extended sources, namely the sum of the experimental

point sources and the volume scattering sources. The underdetermined nature of the source problems directs us toward a data-domain implementation. In this case, the volume scattering sources are computed by propagating backward in time the weighted data residuals by the inverse data-domain Hessian and hence represent a weighted form of the so-called FWI adjoint wavefields. Then, ES-FWI updates the model parameters from these extended wavefields with two possible implementations based on alternating directions or variable projection (van Leeuwen and Herrmann, 2016). From the optimization viewpoint, this bivariate inversion for extended wavefields and subsurface parameters is implemented with penalty-like methods where the FWI data misfit function is augmented with the source misfit function (van Leeuwen and Herrmann, 2013). The source residuals or wave-equation errors represent the volume scattering source described above. The alternating-direction implementation of ES-FWI leads to the following approximate inverse of the extended Born modeling operator:

$$\bar{\mathbf{B}}^{\dagger}[\mathbf{m}^k] = \mathbf{W}_{model}[\mathbf{m}^k]\bar{\mathbf{B}}^{T}[\mathbf{m}^k]\mathbf{W}_{data}[\mathbf{m}^k]. \tag{1}$$

where $\mathbf{m}^k$ represents the initial FWI model at iteration k, $\bar{\mathbf{B}}[\mathbf{m}^k]$ is the extended Born modeling operator, $(\cdot)^T$ and $(\cdot)^{\dagger}$ denote the adjoint and the approximate inverse of $(\cdot)$. In ES-FWI, the only difference between the Born modeling operator $\mathbf{B}$ and its extended form $\bar{\mathbf{B}}$ is that the extended wavefields replace the background wavefields in the virtual sources of the partial derivative data. The model-domain operator $\mathbf{W}_{model}$ is the inverse diagonal pseudo-Hessian of Shin et al. (2001) while the data-domain weighting operator is the inverse data-domain Hessian of the scattering source problem. It results from this analysis that the full model-domain GN Hessian has been decomposed into two terms: a simple diagonal source-side Hessian and a receiver-side data-domain Hessian. These two Hessians deconvolve the virtual sources and the data residuals in the gradient. In this study, we propose to adapt the approximate GN direction developed in the frame of ES-FWI, equation 1, to classical (reduced-space) FWI. The adaptation simply consists of replacing the extended wavefields in the virtual sources of the Born operator with the background wavefields. We assess our GN Hessian implementation as an approximate GN descent direction as such or as improved inputs for preconditioned l-BFGS where the inputs are the weighted gradient by the inverse data-domain Hessian and the inverse diagonal pseudo-Hessian as a preconditioner.

If we set this analysis in the context of the above review, we find the decomposition shown by equation 1 in the approach of Hou and Symes (2015, their equation 1) although the two weighting operators rely on different approaches. The adaptation of the Hessian decomposition to classical FWI by removing the features that extend the search space in $\mathbf{W}_{model}$ is also similar to the approach of Hou and Symes (2016). The idea of introducing a parameter-dependent data-domain weighting operator in the data misfit function to transfer some of its effects in the gradient is also present in the generalized LS ray-Born inversion. While $\mathbf{W}_{model}$ doesn't generate any computational overheads, $\mathbf{W}_{data}$ does. In this study, we approximate the inverse data domain Hessian with a data-domain matching filter following the approach of Liu and Peter (2018); Liu et al. (2019). However, instead of using a 1D filter, we use a 2D nonstationary Gabor filter to represent more accurately the nonstationarity of seismic arrivals in time and offset (Guo et al., 2024). We estimate these matching filters with a data-to-data fitting approach similar to the image-to-image fitting approaches of Rickett (2003); Guitton (2004). The estimation of these matching filters requires two extra simulations (one backward and one forward) per source at each FWI iteration to perform the Hessian-vector product.

In the subsequent sections, we first review the GN Hessian decomposition for FWI. This review is supplemented by Appendix A, which reviews the key principles of ES-FWI that inspired this study. Then, we analyze separately with comprehensive numerical tests the individual effect of the source-side pseudo-Hessian, the receiver-side data-domain Hessian, and the combination of them on the convergence speed, the accuracy of the reconstructed model, and the resilience of the inversion to the accuracy of the initial model. We assess our generalized FWI with the (preconditioned) steepest-descent and the l-BFGS methods. The final section discusses the main inferences drawn from the numerical results revealing the key role of the inverse data domain Hessian in mitigating nonlinearity issues. Finally, we draw some conclusions and perspectives.

THEORY

Classical FWI with model-domain GN Hessian

The cost function of classical time-domain FWI is defined as

$$\phi(\mathbf{m}) = \sum_s \phi_s(\mathbf{m}) = \frac{1}{2}\sum_s \|\mathbf{P}_s\mathbf{u}_s(\mathbf{m}) - \mathbf{d}_s^*\|_2^2, \tag{2}$$

where s denotes the source index, $\mathbf{d}_s^* \in \mathbb{R}^{n_r \times n_t}$ the recorded data for source s, $\mathbf{u}_s \in \mathbb{R}^{3\times m\times n_t}$ the simulated wavefields triggered by source s, and the observation operator $\mathbf{P}_s \in \mathbb{R}^{(n_r\times n_t)\times(3\times m\times n_t)}$ samples $\mathbf{u}_s$ at receivers, n_r is the number of receivers, n_t is the number time sampling, m is the number of model parameters. The incident wavefields $\mathbf{u}_s$ satisfies the wave equation: $\mathbf{u}_s(\mathbf{m}) = \mathbf{A}(\mathbf{m})^{-1}\mathbf{b}_s^*$ where $\mathbf{b}_s^*$ is the experimental source and $\mathbf{A}(\mathbf{m})$ is the time-domain first-order velocity-stress wave-equation operator (Guo et al., 2024). Usually, gradient-based iterative methods are used to update the model parameters at iteration k as

$$\mathbf{m}^{k+1} = \mathbf{m}^k + \alpha_k\mathbf{p}^k = \mathbf{m}^k + \delta\mathbf{m}^k, \tag{3}$$

where $\alpha_k \in \mathbb{R}_+$ is the step length, $\mathbf{p}^k$ is the descent direction, and $\delta\mathbf{m}^k$ is the model perturbation. The descent direction $\mathbf{p}^k$ satisfies the following normal equation:

$$\sum_s \mathbf{H}_s(\mathbf{m}^k)\mathbf{p}^k = -\sum_s \mathbf{g}_s(\mathbf{m}^k), \tag{4}$$

where $\mathbf{H}_s$ and $\mathbf{g}_s$ denote the Hessian and the gradient of the misfit function for the source s. The gradient of the misfit function at $\mathbf{m} = \mathbf{m}^k$ is given by

$$\mathbf{g}_s(\mathbf{m}^k) = \mathbf{J}_s(\mathbf{m}^k)^T\delta\mathbf{d}_s^*(\mathbf{m}^k) = \Big(\mathbf{L}(\mathbf{m}^k)\mathbf{u}_s(\mathbf{m}^k)\Big)^T \mathbf{S}_s(\mathbf{m}^k)^T\delta\mathbf{d}_s^*(\mathbf{m}^k) \tag{5}$$

$$= \mathbf{f}_s(\mathbf{m}^k)^T\mathbf{S}_s(\mathbf{m}^k)^T\delta\mathbf{d}_s^*(\mathbf{m}^k), \tag{6}$$

where $\mathbf{J}_s(\mathbf{m}^k) = \mathbf{S}_s(\mathbf{m}^k)\mathbf{L}(\mathbf{m}^k)\mathbf{u}_s(\mathbf{m}^k)$ is the sensitivity matrix, $\delta\mathbf{d}_s^*(\mathbf{m}^k) = \mathbf{d}_s^* - \mathbf{P}_s\mathbf{u}_s(\mathbf{m}^k)$ are the data residuals (the virtually measured scattered data), $\mathbf{S}_s(\mathbf{m}^k) = \mathbf{P}_s\mathbf{A}(\mathbf{m}^k)^{-1}$ is the modeling operator, $\mathbf{L}(\mathbf{m}^k) = \partial\mathbf{A}(\mathbf{m}^k)/\partial\mathbf{m}$ is the radiation pattern matrix, and $\mathbf{f}_s(\mathbf{m}^k) = \mathbf{L}(\mathbf{m}^k)\mathbf{u}_s(\mathbf{m}^k)$ is the virtual source. Finally, $\mathbf{S}_s(\mathbf{m}^k)^T\delta\mathbf{d}_s^*(\mathbf{m}^k)$ is the adjoint wavefield. The expression 6 highlights that the ith entry of the gradient is computed by taking the scalar product between the ith virtual source and the adjoint wavefield.

The GN Hessian of the misfit function 2 at $\mathbf{m} = \mathbf{m}^k$ is given by

$$\mathbf{H}_s^{GN}(\mathbf{m}^k) = \mathbf{J}_s(\mathbf{m}^k)^T \mathbf{J}_s(\mathbf{m}^k) = \mathbf{f}_s(\mathbf{m}^k)^T \mathbf{S}_s(\mathbf{m}^k)^T \mathbf{S}_s(\mathbf{m}^k) \mathbf{f}_s(\mathbf{m}^k). \tag{7}$$

This leads to the GN normal equation for the descent direction $\mathbf{p}^k$:

$$\sum_s \mathbf{H}_s^{GN}(\mathbf{m}^k)\mathbf{p}^k \approx -\sum_s \mathbf{g}_s(\mathbf{m}^k), \tag{8}$$

where $\mathbf{p}^k$ is given by

$$\mathbf{p}^k = -\frac{\sum_s \mathbf{f}_s(\mathbf{m}^k)^T \mathbf{S}_s(\mathbf{m}^k)^T \delta\mathbf{d}_s^*(\mathbf{m}^k)}{\sum_s \mathbf{f}_s(\mathbf{m}^k)^T \mathbf{S}_s(\mathbf{m}^k)^T \mathbf{S}_s(\mathbf{m}^k) \mathbf{f}_s(\mathbf{m}^k)} \tag{9}$$

The linear equation 8 can be solved with a few iterations of the CG method in the framework of the truncated-Newton method, where the Hessian-vector product is computed with the matrix-free second-order adjoint-state method (Métivier et al., 2013).

Generalized FWI with decomposed GN Hessian

Here, we provide an alternative implementation of the GN iteration to make it more computationally efficient. This implementation is inspired by the extended-source (ES) FWI whose principles have been introduced in the previous section and are reviewed more formally in Appendix A (Gholami et al., 2022; Operto et al., 2023; Guo et al., 2024). We introduce a generalized or weighted form of the FWI misfit function ϕ by implementing a data-domain weighting operator formulated as the inverse Hessian of the scattering source $\delta\mathbf{b}$ problem (Appendix A). At a given FWI iteration k, $\delta\mathbf{b}$ refers to the volume scattering source formed by the interaction of the (unknown) true wavefields with the (unknown) sought model perturbation such that the scattered wavefield triggered by this source when added to the background wavefield would give the true wavefield, equations (A-1)-(A-3). Estimating wavefields that approximate as well as possible the true wavefields via the estimation of $\delta\mathbf{b}$ is the cornerstone of ES-FWI. This scattering source can be estimated by fitting the data residuals in an LS sense, equations (A-4)-(A-6). The ES-FWI formulation shows that the adjoint wavefield of FWI should be interpreted as the adjoint approximation of $\delta\mathbf{b}$. Therefore, we propose to implement a more accurate LS approximation of $\delta\mathbf{b}$ in the gradient of the FWI misfit function in place of the adjoint approximation. This can be implemented by using the inverse Hessian of the $\delta\mathbf{b}$ problem, see equation A-6, as a weighting operator of the data misfit function as above mentioned. Let us stress that the model-domain GN Hessian of FWI embeds implicitly the Hessian of the $\delta\mathbf{b}$ problem because the partial derivative data involve wavepaths connecting the scatterers to the receivers. In our approach, the weighting of the data misfit function by the inverse receiver-side Hessian aims at simplifying (diagonalizing) the GN model-domain Hessian of FWI by transferring some of its effects in the gradient. This GN Hessian decomposition is justified mathematically by the iteration of the alternating-direction implementation of ES-FWI reviewed in Appendix A, equation A-11. Here, we simply adapt this formulation to the classical reduced-space FWI by replacing the extended wavefields with the background wavefields in the virtual sources of the partial derivative data. By doing so, our motivation is to propose a more computationally-efficient implementation of GN iteration for FWI without the

computational overhead of ES-FWI generated by the computation of the extended wavefields. Hereafter, we introduce the new decomposed GN iteration for FWI heuristically. The reader is referred to Appendix A for its mathematical justification in the frame of the alternating-direction ES-FWI.

At iteration k, the generalized FWI misfit function ϕ^g is given

$$\phi_k^g(\mathbf{m}) = \sum_s \phi_{k_s}^g(\mathbf{m}) = \frac{1}{2}\sum_s \|\mathbf{P}_s\mathbf{u}_s(\mathbf{m}) - \mathbf{d}_s^*\|^2_{\mathbf{H}_s^d(\mathbf{m}^k)^{-1}}, \tag{10}$$

where the superscript g stands for generalized, $\mathbf{H}_s^d(\mathbf{m}^k) = \left(\mathbf{S}_s(\mathbf{m}^k)\mathbf{S}_s(\mathbf{m}^k)^T + \mu\mathbf{I}\right)$ is the damped (damping term μ) data-domain Hessian of the $\delta\mathbf{b}$ problem computed in $\mathbf{m}^k$, equation A-6, and we recall that $\| \bullet \|^2_{\mathbf{Q}} = \bullet^T\mathbf{Q}\bullet$. The gradient and the GN Hessian of ϕ^g at $\mathbf{m} = \mathbf{m}^k$ are given by

$$\mathbf{g}_s^g(\mathbf{m}^k) = \mathbf{J}_s(\mathbf{m}^k)^T\mathbf{H}_s^d(\mathbf{m}^k)^{-1}\delta\mathbf{d}_s^*(\mathbf{m}^k) = \mathbf{f}_s(\mathbf{m}^k)^T\mathbf{S}_s(\mathbf{m}^k)^T\mathbf{H}_s^d(\mathbf{m}^k)^{-1}\delta\mathbf{d}_s^*(\mathbf{m}^k), \tag{11}$$

and

$$\begin{aligned}
\mathbf{H}_s^{g^{GN}}(\mathbf{m}^k) &= \mathbf{J}_s(\mathbf{m}^k)^T\mathbf{H}_s^d(\mathbf{m}^k)^{-1}\mathbf{J}_s(\mathbf{m}^k) \\
&= \mathbf{f}_s(\mathbf{m}^k)^T\mathbf{S}_s(\mathbf{m}^k)^T\left(\mathbf{S}_s(\mathbf{m}^k)\mathbf{S}_s(\mathbf{m}^k)^T + \mu\mathbf{I}\right)^{-1}\mathbf{S}_s(\mathbf{m}^k)\mathbf{f}_s(\mathbf{m}^k) \\
&\approx \mathbf{f}_s(\mathbf{m}^k)^T\mathbf{f}_s(\mathbf{m}^k).
\end{aligned} \tag{12}$$

The expression in equation 12 corresponds to the diagonal pseudo-Hessian of Shin et al. (2001) formed by the squared amplitudes of the virtual sources. The approximation in Equation 12 results from the (wrong) assumption that $\mathbf{S}_s(\mathbf{m}^k)$ is invertible:

$$\mathbf{S}_s(\mathbf{m}^k)^T\left(\mathbf{S}_s(\mathbf{m}^k)\mathbf{S}_s(\mathbf{m}^k)^T\right)^{-1}\mathbf{S}_s(\mathbf{m}^k) = \mathbf{I}. \tag{13}$$

Using this approximation, the GN iteration of GFWI is given by

$$\mathbf{p}^k = -\frac{\sum_s \mathbf{g}_s^g(\mathbf{m}^k)}{\sum_s \mathbf{H}_s^{g^{GN}}(\mathbf{m}^k)} = -\frac{\sum_s \mathbf{f}_s(\mathbf{m}^k)^T\mathbf{S}_s(\mathbf{m}^k)^T\mathbf{H}_s^d(\mathbf{m}^k)^{-1}\delta\mathbf{d}_s^*(\mathbf{m}^k)}{\sum_s \mathbf{f}_s(\mathbf{m}^k)^T\mathbf{f}_s(\mathbf{m}^k)}, \tag{14}$$

One can readily check that the only differences between the approximate GN directions for FWI, equation 14, and ES-FWI, A-11, are the incident wavefields involved in the virtual sources, namely the background wavefields $\mathbf{u}_s$ and the extended wavefields $\mathbf{u}_s^e$, respectively. Moreover, the approximation in the ES approach that leads to the descent direction involving a diagonal model-domain Hessian, equation A-11, results from the alternating-direction optimization. The alternated updating of $\mathbf{u}$ and $\mathbf{m}$ linearizes the $\mathbf{m}$ subproblem around the reconstructed wavefields, i.e. the extended wavefields reconstructed from the solution of the rank-deficient source problem are assumed to be the true wavefields during parameter updating. This assumption can be reformulated by saying that $\mathbf{S}_s$ is invertible, namely the source problem is made full rank by deploying receivers across the entire subsurface domain. In this case, the true wavefields can be indeed computed exactly from one source and one frequency by virtue of the bi-linearity of the wave equation (Aghamiry et al., 2019). The assumption that $\mathbf{S}_s$ is invertible is precisely the one we made to diagonalize the Hessian in the model domain, equation 12. This comment aims to highlight the consistency between the approximate GN descent direction for FWI developed above and the counterpart developed for alternating-direction ES-FWI in Appendix A.

Implementation of decomposed GN Hessian

The source-side pseudo-Hessian can be computed on the fly without extra computational overhead with a damping term to prevent unstable parameter updates at large depths:

$$\mathbf{H}_s^{GN}(\mathbf{m}^k) = \mathbf{f}_s(\mathbf{m}^k)^T\mathbf{f}_s(\mathbf{m}^k) + \lambda\mathbf{I}, \tag{15}$$

where λ is the damping parameter, which can be set to a small fraction of the maximum diagonal coefficient (e.g. Ravaut et al., 2004, their figures 14 and 15). The accurate and efficient computation of the source-dependent data-domain Hessians $\mathbf{H}_s^d(\mathbf{m}^k)$ is more complex since it involves a multidimensional deconvolution. We approximate the inverse of these data-domain Hessians with matching filters as proposed by Guo et al. (2024). This first requires a backward and forward simulation per source to apply the data-domain Hessian on the data residuals:

$$\delta\mathbf{d}_s^b(\mathbf{m}^k) = \mathbf{S}_s(\mathbf{m}^k)\mathbf{S}_s(\mathbf{m}^k)^T\delta\mathbf{d}_s^*(\mathbf{m}^k) \tag{16}$$

Then, we estimate the matching filter $\mathbf{F}_s$ the best matches the data residuals in a LS sense:

$$\mathbf{F}_s\delta\mathbf{d}_s^b(\mathbf{m}^k) \approx \delta\mathbf{d}_s^*(\mathbf{m}^k), \tag{17}$$

Here, we use multi-dimensional non-stationary Gabor matching filters, which are estimated in the frequency domain, to better capture the times and slopes of locally-coherent events in the seismic gathers (Guo et al., 2024). The FWI algorithm with decomposed GN Hessian is outlined in Algorithm 1.

Algorithm 1 Time-domain FWI with decomposed GN direction.

Input: $\mathbf{m}^0$, $\mathbf{d}^*$ and $\mathbf{b}^*$
while convergence criteria not satisfied **do**
  for $s = 1,\ N_s$ **do**
    Forward wavefield $\mathbf{u}_s(\mathbf{m}^k) = \mathbf{A}(\mathbf{m}^k)^{-1}\mathbf{b}_s^*$ and $\delta\mathbf{d}_s^*(\mathbf{m}^k) = \mathbf{d}_s^* - \mathbf{P}_s\mathbf{u}_s(\mathbf{m}^k)$.
    Solve the data-domain multi-dimensional deconvolution problem $\delta\mathbf{d}_s^d(\mathbf{m}^k) = \mathbf{H}_s^d(\mathbf{m}^k)^{-1}\delta\mathbf{d}_s^*(\mathbf{m}^k)$.
    Adjoint wavefield $\mathbf{v}_s(\mathbf{m}^k) = \mathbf{S}_s(\mathbf{m}^k)^T\delta\mathbf{d}_s^d(\mathbf{m}^k)$.
  end for
  Approximate decomposed GN direction $\mathbf{p}^k = -\frac{\sum_s\langle\mathbf{L}(\mathbf{m}^k)\mathbf{u}_s(\mathbf{m}^k),\ \mathbf{v}_s(\mathbf{m}^k)\rangle}{\sum_s\langle\mathbf{L}(\mathbf{m}^k)\mathbf{u}_s(\mathbf{m}^k),\ \mathbf{L}(\mathbf{m}^k)\mathbf{u}_s(\mathbf{m}^k)\rangle}$.
  Update model parameters $\mathbf{m}^{k+1} = \mathbf{m}^k + \delta\mathbf{m}^k$ with SD or l-BFGS algorithms.
  $k = k + 1$,
end while

NUMERICAL TEST

Marmousi II model: The convergence of FWI and GFWI

Experimental setup

We first validate the algorithm with the Marmousi II model (Figure 1a). We build three initial models of decreasing accuracy by smoothing the true model with Gaussian filters

of horizontal and vertical correlation lengths 250 m (model S1), 350 m (model S2), and 450 m (model S3) (Figure 1b-d), respectively. The surface stationary-recording acquisition involves 68 hydrophones on the seabed and 227 pressure sources at 50 m depth. We exploit the reciprocity of Green functions to process sources as reciprocal receivers and vice versa to mitigate the computational cost. A free-surface boundary condition is set on the surface while a perfectly matched layer condition is implemented along the remaining edges of the grid. We perform wave simulation in the time domain with a $\mathcal{O}(\Delta t^2, \Delta x^4)$ staggered-grid finite-difference stencil applied on the 2D velocity-stress acoustic wave equation (Virieux, 1984), while the sources and the receivers are positioned at arbitrary positions with Kaiser-windowed Sinc functions (Hicks, 2002). The source function is a Ricker wavelet with a 4 Hz dominant frequency, and frequencies below 2 Hz are muted. We apply an all-at-once inversion in the [2; 12] Hz frequency band. First, we assess the data match at the first iteration in Figure 2. The difference between the kinematic mismatches between seismograms computed in the true and smoothed models S1, S2, and S3 are relatively subtle when looking at the first arrivals. However, a close examination of the late energetic arrivals at long offsets shows that phase shifts increased from S1 to S3 models with the potential risk of trapping FWI in spurious minima. We compare the results of FWI (equation 2) and GFWI (equation 10) using the SD and the l-BFGS optimization methods implemented in the SEISCOPE optimization toolbox (Métivier and Brossier, 2016). For FWI and GFWI and the two optimization algorithms (SD, l-BFGS), we use or not the diagonal pseudo-Hessian of equation 12 as a preconditioner. This means that, when GFWI is implemented with the SD method without preconditioner, we disregard the diagonal pseudo-Hessian while keeping the inverse data-domain Hessian in the gradient, equation 14. Conversely, when we implement GFWI with the preconditioned SD algorithm, both model-domain and data-domain Hessians are used and hence the preconditioned SD iterations can be viewed as approximate GN iterations. In the following, we label the different test configurations with the following acronyms: (SD/l-BFGS)-[p](FWI/GFWI) depending on the chosen optimization algorithm (SD *vs* l-BFGS), the chosen misfit function (FWI *vs* GFWI misfit function), and whether or not preconditioner p is used. It is also important to note that the weighting operator for the cost function of GFWI depends on the model at the current iteration, thus the algorithm for such updates falls outside the scope of standard optimization theory. We proceed under the assumption that the change in the cost function can be neglected from one iteration to the next (Fu and Symes, 2017), albeit without rigorous proof, and numerical tests validate the feasibility of this approach. In all cases, the maximum number of iterations is 50. However, the inversion process is terminated early if the linear search fails. We apply the bound constraints without additional regularization during the inversion. The damping parameter λ is set to $1e^{-3}$, equation 15.

FWI and GFWI results

We start with the results obtained with the more accurate S1 model. The raw and the preconditioned gradients at the first iteration, the final models, velocity logs, and the convergence curves are shown in Figures 3, 4, 5, and 6, respectively. The raw and preconditioned gradients at the first iteration for FWI and GFWI highlight the contribution of each component of the GN Hessian (Figures 3). The raw FWI gradient, equation 6, shows unbalanced perturbations with depth and numerical artifacts (acquisition footprint) resulting from the relatively sparse receiver (reciprocal source) layout (Figure 3a). These artifacts

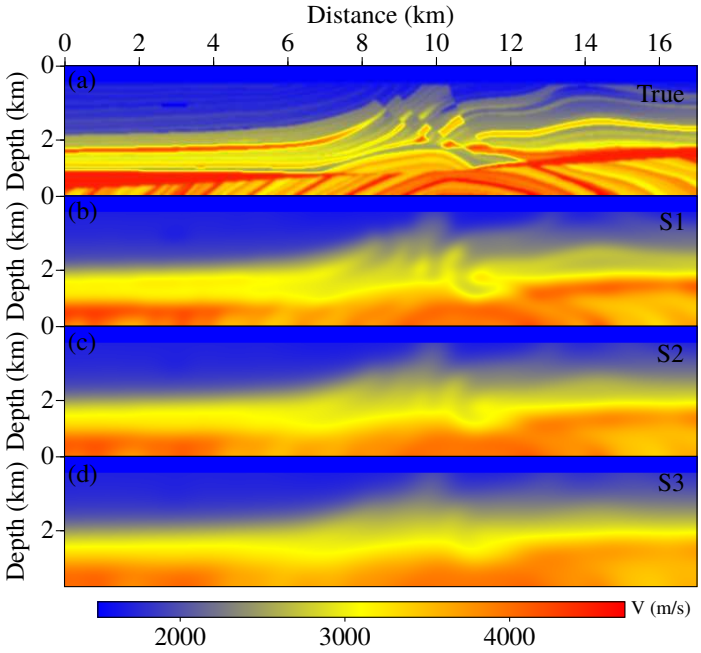

Figure 1: Marmousi II. (a) True Marmousi II model. (b-d) Smooth initial model S1 (b), S2 (c), S3 (d). Correlation lengths of the Gaussian smoother are 250 m (b), 350 m (c), and 450 m (d), respectively.

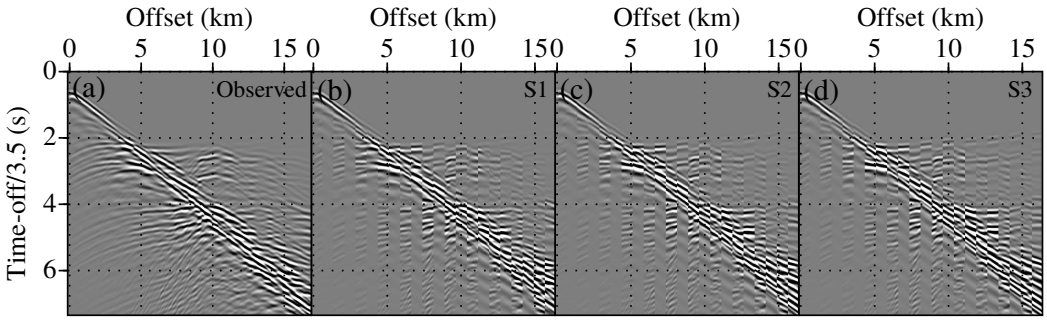

Figure 2: Marmousi II. (a) Observed data. (b-d) Interleaved data between observed data and simulated data with the model (b) S1, (c) S2, and (d) S3.

manifest as numerical coherent pollution in depth resulting from the adjoint simulation of the data residuals. The preconditioned FWI gradient provides better-balanced perturbations with depth as expected (Figure 3b). The raw GFWI gradient, equation 11, (Figure 3c) minimizes the artifacts seen in the raw FWI gradient, hence highlighting the contribution of the data-domain Hessian (Figure 3a). For example, check the small inclusion at 3 km distance and 1 km depth. Finally, the preconditioned GFWI gradient or GFWI descent direction, equation 14, (Figure 3d) provides both the best amplitude balancing in-depth and the best focusing of the structures, providing a first validation of the proposed approach.

The final models obtained with the different optimization schemes are shown in Figure 4. Overall, all of the models show a satisfying accuracy from the qualitative viewpoint. We provide the model mean squared error (MSE) in each panel of Figure 4 to rank the quality of each model more quantitatively. Furthermore, Figure 5 presents a direct comparison between the true model and the reconstructed ones along several vertical profiles. From this comparison, we see that the amplitudes of the sharp contrasts (arrows in Figure 5) are better reconstructed by the preconditioned algorithms relative to the unpreconditioned ones and that l-BFGS outperforms SD as expected. Finally, one can jointly analyze the convergence speed of the inversions and the accuracy of the reconstructed models as provided by their MSE in Figure 6. It is worth noting that, for both FWI and GFWI, we plot the (unweighted) LS data misfit function curve versus iterations for a fair comparison between the two approaches. Indeed, the LS data misfit function of FWI, equation 2, should not be confused with the weighted LS data misfit function of GFWI, equation 10. The basic conclusions that can be drawn from Figures 4, 5 and 6 are the following: (1) SD FWI and SD GFWI (gray and blue circles) provide the slowest convergence speeds and the worst models, the latter being slightly more accurate than the former (Figure 4a1, c1). This highlights that the pseudo-Hessian preconditioner has a dominant role when the starting model is accurate. (2) SD p-GFWI (red circles) and SD p-FWI (black circles) have comparable convergence speeds, although the former exhibits a smoother trend. Moreover, the SD p-GFWI model (red circles) is slightly more accurate than the SD p-FWI model (Figure 4b1, d1). This confirms that that the pseudo-Hessian preconditioner has a dominant role when the starting model is accurate. Moreover, the SD p-GFWI model (red circles) is very similar to the l-BFGS FWI model and is also quite comparable with the l-BFGS p-FWI model. This suggests the SD p-GFWI provides a fairly good approximation of the GN descent direction. (3) l-BFGS GFWI and lBFGS p-GFWI (blue and red triangles) provide both the best models and convergence speeds, the latter achieving the best results on both aspects. They significantly outperform the FWI results obtained with l-BFGS (gray and black triangles). This provides a first validation that p-GFWI provides a reliable gradient and preconditioner for l-BFGS (Figure 4a2-b2 *vs.* Figure 4c2-d2).

Next, we move to the results obtained with the intermediate S2 starting model. The figure of the first gradients mainly highlights how the preconditioned FWI gradient computed in the S2 model (Figure 7b) is noisier than the counterpart computed in the more accurate starting model S1 (Figure 3b, arrow) while the differences between the preconditioned GFWI gradients computed in the S1 and S2 models look more similar (Figure 3d and 7d). The reconstructed models from the S2 starting model remain of acceptable quality (Figure 8) and show the same trend as in Figure 4. However, the direct comparison of velocity logs (Figure 9) reveals more significant differences between the different models compared to those obtained with the S1 initial model (Figure 5). The joint analysis of the convergence curves and the MSE curves further highlight these differences that indicate the importance

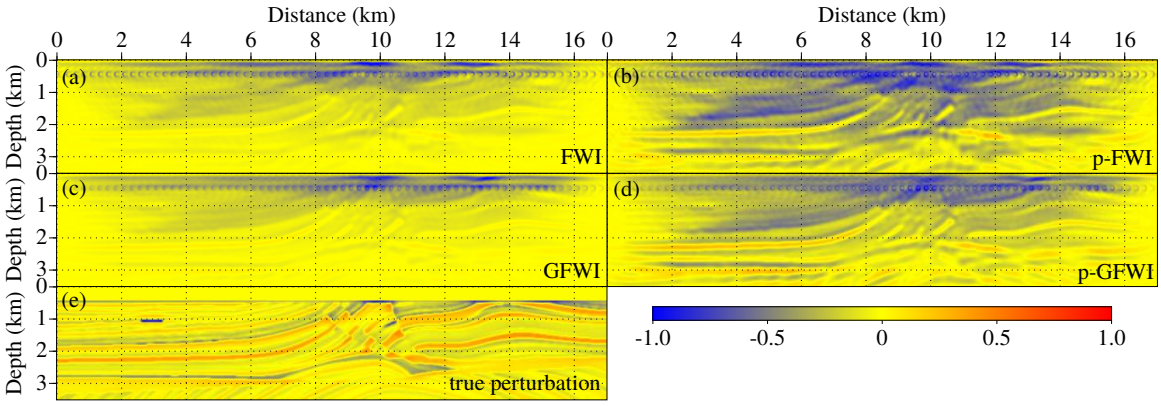

Figure 3: Marmousi II. (Preconditioned) gradient of FWI and GFWI misfit functions at first iteration for S1 initial model. (a) Raw gradient of FWI misfit function, equation 2. (b) Preconditioned gradient of FWI misfit function. The preconditioner is diagonal pseudo Hessian given by auto-correlation of virtual sources, equation 12. (c) Raw gradient of GFWI misfit function, equation 10. (d) Preconditioned gradient of GFWI misfit function by pseudo-Hessian. This can be viewed as an approximation of the FWI GN descent direction. (e) True perturbation model. Each panel is normalized by its maximum amplitude.

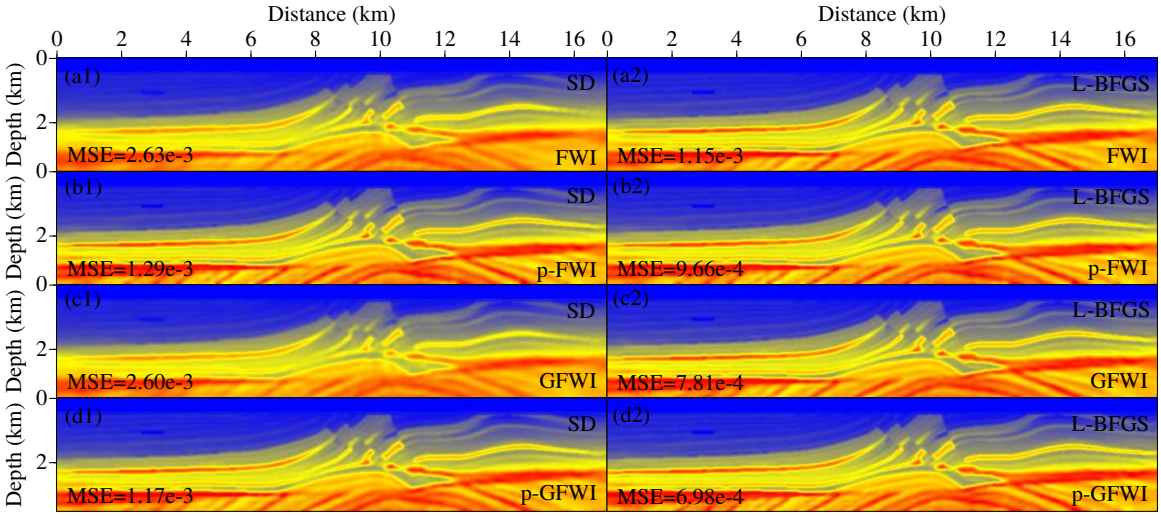

Figure 4: Marmousi II. Reconstructed models from S1 initial model using (a1-d1) SD and (a2-d2) l-BFGS optimization methods. (a-b) FWI (a) without and (b) with pseudo-Hessian preconditioner. (c-d) GFWI (c) without and (d) with pseudo-Hessian preconditioner. MSE is shown in each panel.

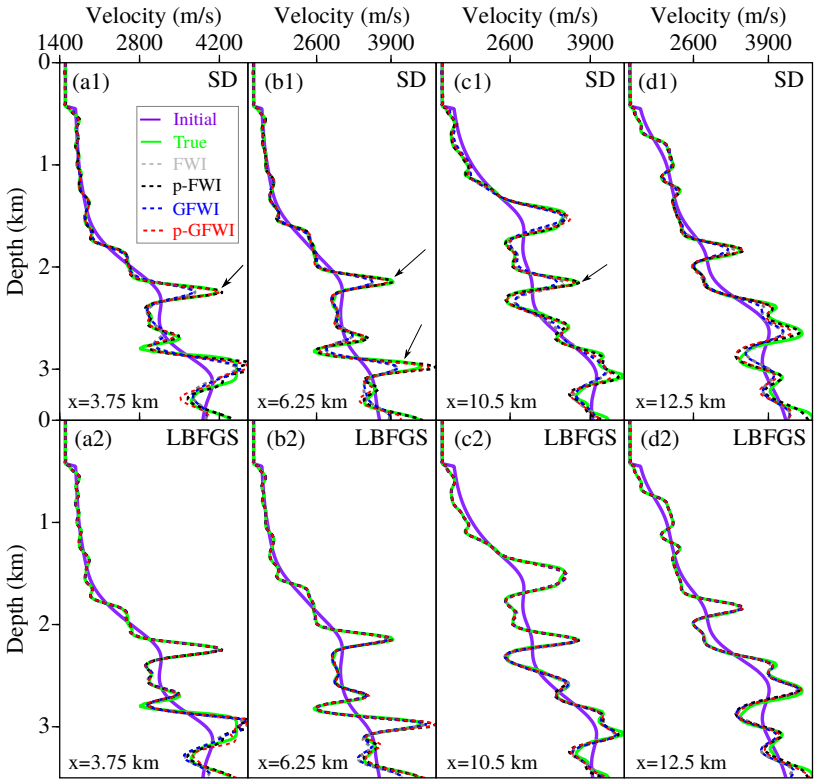

Figure 5: Marmousi II. Direct comparison of the true model (green), initial model (purple), reconstructed models from S1 initial model using (a1-d1) SD and (a2-d2) *l*-BFGS optimization methods. (a-b) FWI without (gray) and with (black) pseudo-Hessian preconditioner. (c-d) GFWI without (blue) and with (red) pseudo-Hessian preconditioner. The arrows note the well reconstruction of sharp boundary when decomposed GN Hessian is applied.

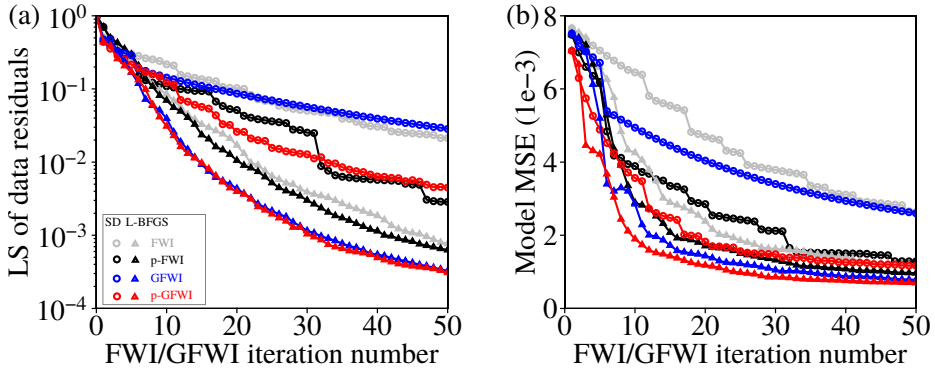

Figure 6: Marmousi II. (a) Convergence curves of normalized LS norm of data residuals for S1 initial model using SD method (circles) and *l*-BFGS method (triangles). FWI without pseudo-Hessian preconditioner (gray) and with pseudo-Hessian preconditioner (black). GFWI without pseudo-Hessian preconditioner (blue) and with pseudo-Hessian preconditioner (red). (b) Model MSE for FWI and GFWI with the same convention as (a).

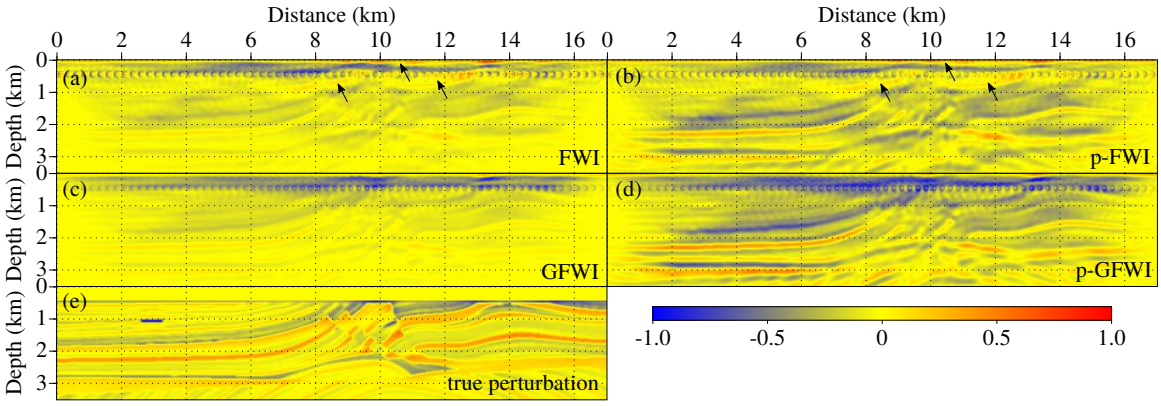

Figure 7: Marmousi II. Same as Figure 3 for S2 starting model.

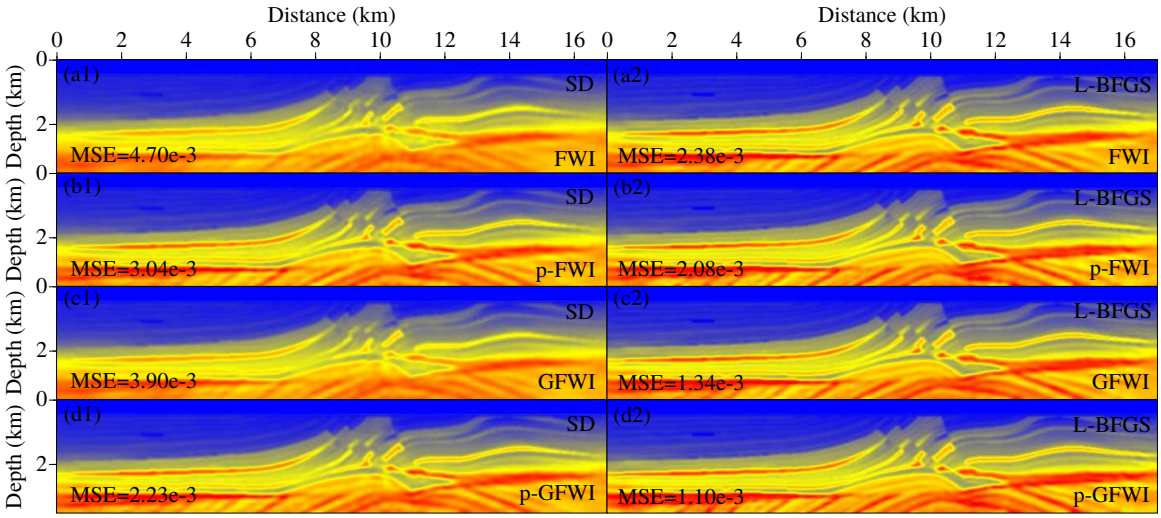

Figure 8: Marmousi II. Same as Figure 4 for S2 starting model.

and the different roles of the two Hessian components (source-side and receiver-side) when the initial model is less accurate (Figure 10). First, SD FWI (gray circles) converges slower than SD p-FWI (black circles) as expected. However, this difference is less than for the S1 model. This might result from the difficulty of updating the deep part of the model fostered by the preconditioner from an inaccurate starting model. Moreover, SD p-GFWI (red circles) improves more significantly the convergence speed and the model quality relative to SD p-FWI (black circles) when considering the inaccurate S2 model instead of the accurate S1 model (compare the relative trends of black circles and red circles in Figures 6 and 10; these curves are closer in Figure 6 than in Figure 10). This suggests that the inverse data-domain Hessian in GFWI (which is absent in SD p-FWI) has a higher impact when the starting model is less accurate. As for the S1 model, l-BFGS GFWI and l-BFGS p-GFWI provide the best convergence and models with a slightly better model for the latter. This further supports that GFWI provides a reliable gradient and preconditioner for l-BFGS.

These conclusions are further supported by the results obtained with the S3 starting model. We show the first raw and preconditioned FWI/GFWI gradients in Figure 11. Compared with the preconditioned FWI gradient computed in the S2 initial model, the

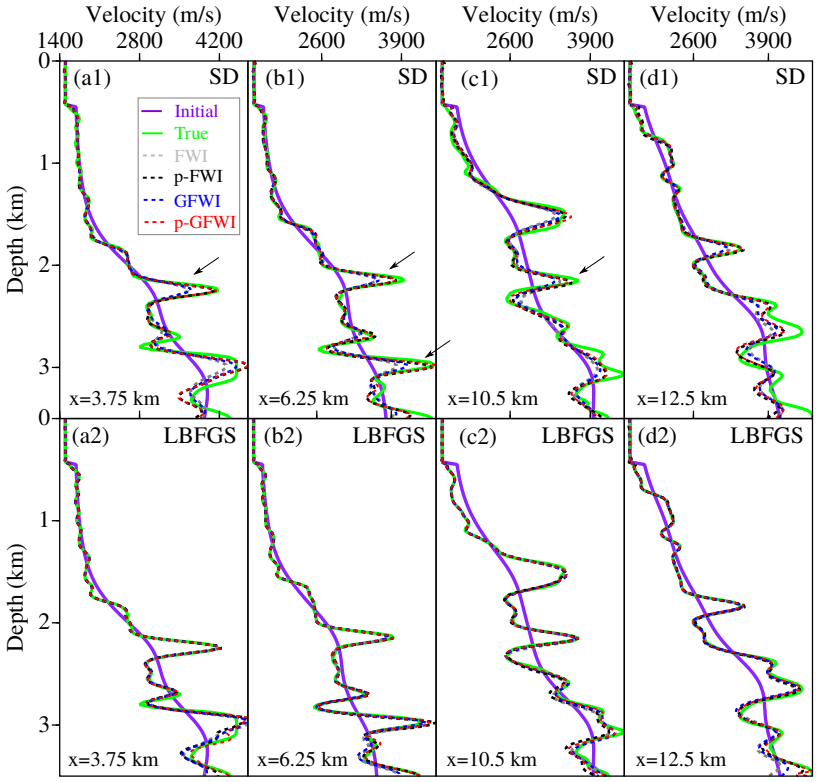

Figure 9: Marmousi II. Same as Figure 5 for S2 starting model.

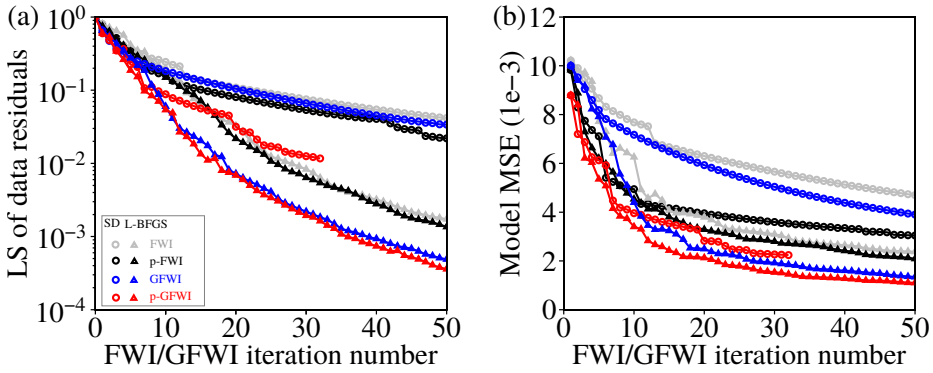

Figure 10: Marmousi II. Same as Figure 6 for S2 starting model.

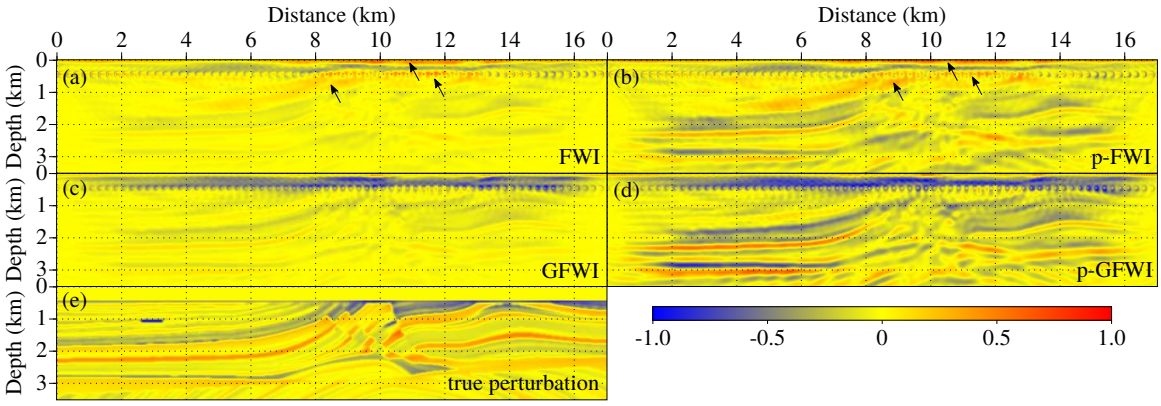

Figure 11: Marmousi II. Same as Figure 3 for S3 starting model. Note that the gradient of the high-velocity noise around the acquisition is depressed by the data-domain Hessian.

one computed in the S3 initial model exhibits more obvious artifacts (Figure 11b, arrow). Conversely, the preconditioned GFWI gradients computed in the S2 and S3 models are more consistent. This confirms that the inverse data domain Hessian has an increasingly important role when the accuracy of the starting model decreases. The contrasted accuracy of the FWI and GFWI gradients is reflected in an obvious way in the final reconstructed models (Figure 12). In this case, only GFWI provides reliable results (Figure 12c1-d1). The strong acquisition footprint and shallow artifacts highlighted in the FWI gradients have hindered the convergence of FWI toward reliable minima (Figure 12a1-b1). One can check in more detail these artifacts in vertical profiles (Figure 13). Moreover, it is worth noting that l-BFGS FWI and l-BFGS p-FWI give the noisier results suggesting that the deconvolution performed by the Hessian in l-BFGS has boosted noise (Figure 12a2-b2). SD p-GFWI provides reliable model validating the decomposed GN Hessian as a more robust alternative than the classical GN Hessian of FWI in case of inaccurate starting models (Figures 12d1 and Figure 14, red circles). The convergence speed achieved by l-BFGS p-GFWI and the accuracy of the recontruted model by l-BFGS p-GFWI (Figures 12d2) remain however significantly better than those achieved by SD p-GFWI hence validating that l-BFGS p-GFWI is the most efficient algorithm (red triangles versus red circles in Figure 14).

GO_3D_OBS synthetic model: The cycle-skipping issue of FWI and GFWI

Experimental setup

To further validate the effect of data-domain Hessian for cycle-skipping issue, we now consider a 2D section of GO_3D_OBS synthetic model to assess the decomposed GN Hessian in the framework of ultra long-offset regional crustal-scale exploration (Figure 15a). This geomodel embeds the main structural units (accretionary wedge, subducting slab, thrusts) characterizing complex subduction zones (Górszczyk and Operto, 2021). The initial model is generated by smoothing the true model with a 2D Gaussian filter with adaptive correlation lengths: The horizontal and vertical correlation lengths are set to $0.7 \times \lambda_{local}$ where λ_{local} denotes the local wavelength (Figure 15b). The OBN acquisition involves 100 OBNs spaced

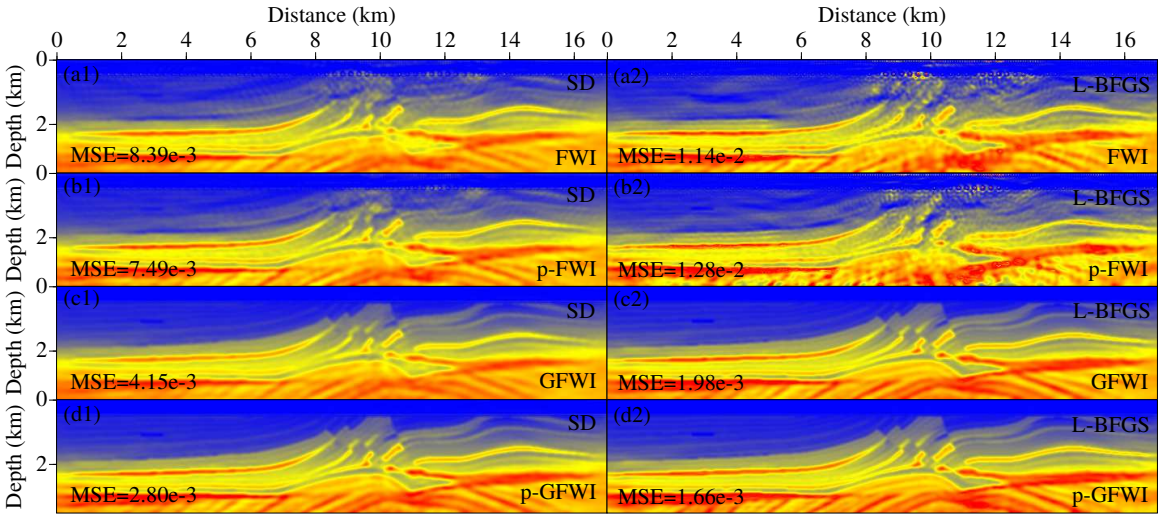

Figure 12: Marmousi II. Same as Figure 4 for S3 starting model.

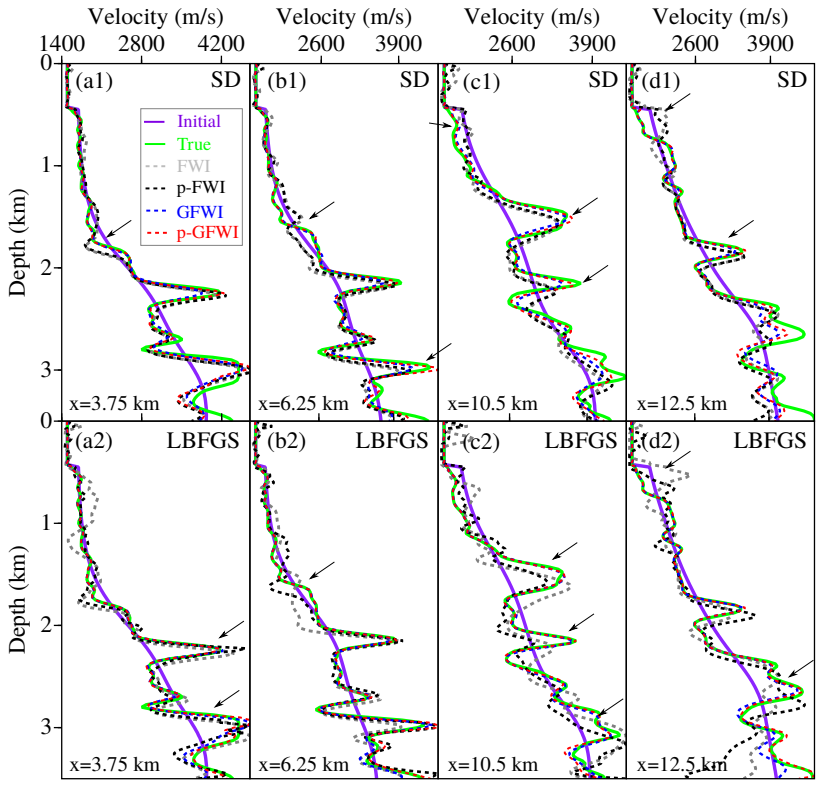

Figure 13: Marmousi II. Same as Figure 5 for S3 starting model.

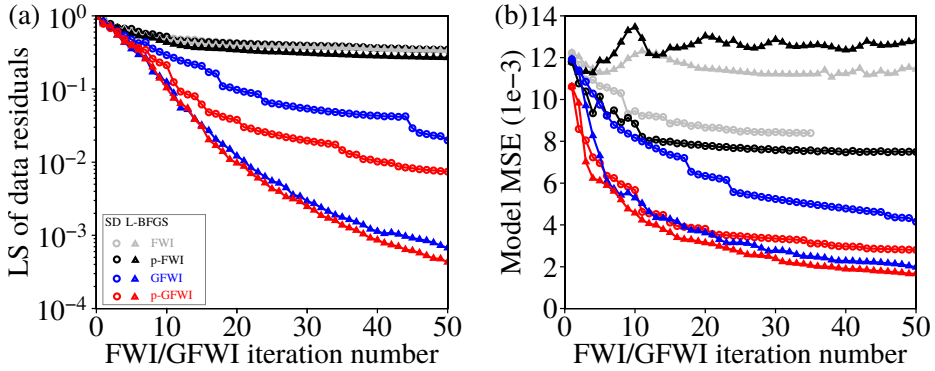

Figure 14: Marmousi II. Same as Figure 6 for S3 starting model.

1 km apart and 1040 explosive sources spaced 100 m apart at a depth of 50 m below the sea level. The source signature is a 2 Hz Ricker wavelet. We conduct the FWI/GFWI using two frequency bands: [1.5; 1.8] Hz and [1.5; 4] Hz. The optimization involves 25 iterations in the first scale and 30 iterations in the second scale. The observed data and simulated data from the initial model, computed for the frequency band [1.5; 4] Hz and including surface multiples, are shown in Figure 16. One can see evident time-shift errors from the interleaved data. Following the previous Marmousi II benchmark, we perform FWI and GFWI with SD and l-BFGS optimization methods using or not pseudo-Hessian preconditioner (Figure 17).

FWI and GFWI results

We perform a comprehensive comparison of the final FWI/GFWI models (Figure 17), velocity logs (Figure 18), and interleaved data as well as data residuals between observed data and simulated data in the final FWI/GFWI models (Figure 19). The final models obtained by SD FWI and SD p-FWI are contaminated by artifacts (Figure 17a1-b1). Some high-frequency artifacts distort the shallow part of the medium in the shallow-water area of the model at around 20 km distance when the pseudo-Hessian preconditioner is not used (Figure 17a1). The pseudo-Hessian preconditioner mitigates these artifacts, suggesting that they might result from nonlinearities generated by the complex interaction between the primaries and the surface multiples in the shallow-water region of the model (Figure 17b1). This speculative statement is motivated by the fact that the pseudo-Hessian preconditioner tends to damp shallow perturbations relative to deeper ones, potentially reducing the impact of nonlinearities caused by complex wave propagation effects in the shallow areas (Ravaut et al., 2004, Their Figures 14 and 15). This is further evidenced by the phase mismatch of early-arrival in Figure 19a1(red circles),e1, which is slightly mitigated when the pseudo-Hessian is applied (Figure 19b1,f1). At greater depths, low-frequency, high-velocity patches appear at 10 km and 60 km distances, which are stronger when the pseudo-Hessian preconditioner is used (Figure 17a1-b1). These deeper artifacts, also visible in Figure 18a-c, may result from cycle skipping and tend to be boosted by the amplitude balancing in-depth performed by the pseudo-Hessian preconditioner as suggested by comparing the data fit at long offset shown in Figures 19a1,e1 and 19b1,f1. Along the same line, these artifacts are even pronounced when l-BFGS is used, due to the deconvolution action of the Hessian performed by l-BFGS (Figure 17a2-b2). A similar pathology was already mentioned in the

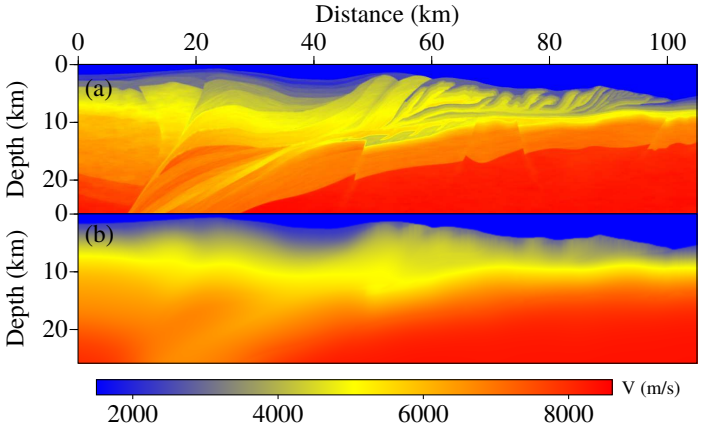

Figure 15: GO_3D_OBS model. (a) True model. (b) Initial model.

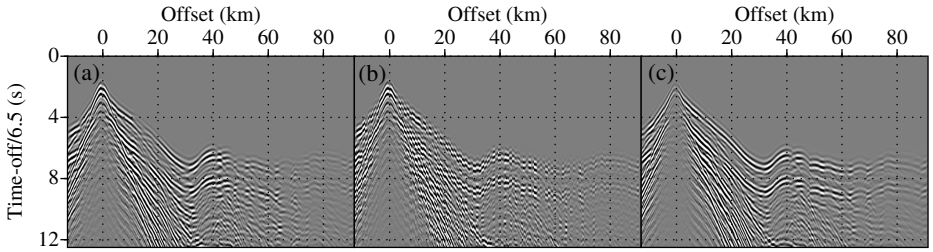

Figure 16: GO_3D_OBS model. (a) Observed data. (b) Interleaved data between observed data and simulated data in the initial model. (c) Data residuals between observed data and simulated data in the initial model.

Marmousi section.

SD GFWI provides better results, although the shallow artifacts are still present to a lower extent in the shallow part of the model at around 10-20 km distance (Figure 17c1), as confirmed by the slight data mismatch in Figure 19c1,g1. In contrast, these artifacts disappear when the pseudo-Hessian preconditioner is used in SD p-GFWI (Figure 17d1), which is supported by the improved data fit in Figure 19d1,h1. The deeper artifacts at 60 km distance are not seen in the SD GWI and SD p-GFWI models (Figure 17c1-d1), suggesting that the action of the data-domain receiver-side Hessian contributes to mitigate the detrimental effects of cycle skipping (Figure 19c1-d1,g1-h1). While l-BFGS FWI fails to provide good model (Figure 17a2), l-BFGS GFWI (Figure 17c2) delivers a better model than SD p-GFWI (Figure 17d1). Note also that l-BFGS GFWI provides a slightly more stable model in the deep part compared to l-BFGS p-GFWI (Figure 17d2). The superiority of the models reconstructed by l-BFGS GFWI and l-BFGS p-GFWI, despite the artifacts shown in the deep part of the latter, is further highlighted by a better data fit achieved by these models (Figure 19c2-d2,g2-h2). The deeper artifacts below 20 km are more apparent in velocity logs (Figure 18d2, blue line *vs.* red line). This study confirm that the best results are obtained by combining GFWI with l-BFGS.

The convergence curves support the above analysis (Figure 20). FWI shows slow convergence (Figure 20a, gray and black symbols) due to the high-amplitude shallow and deep

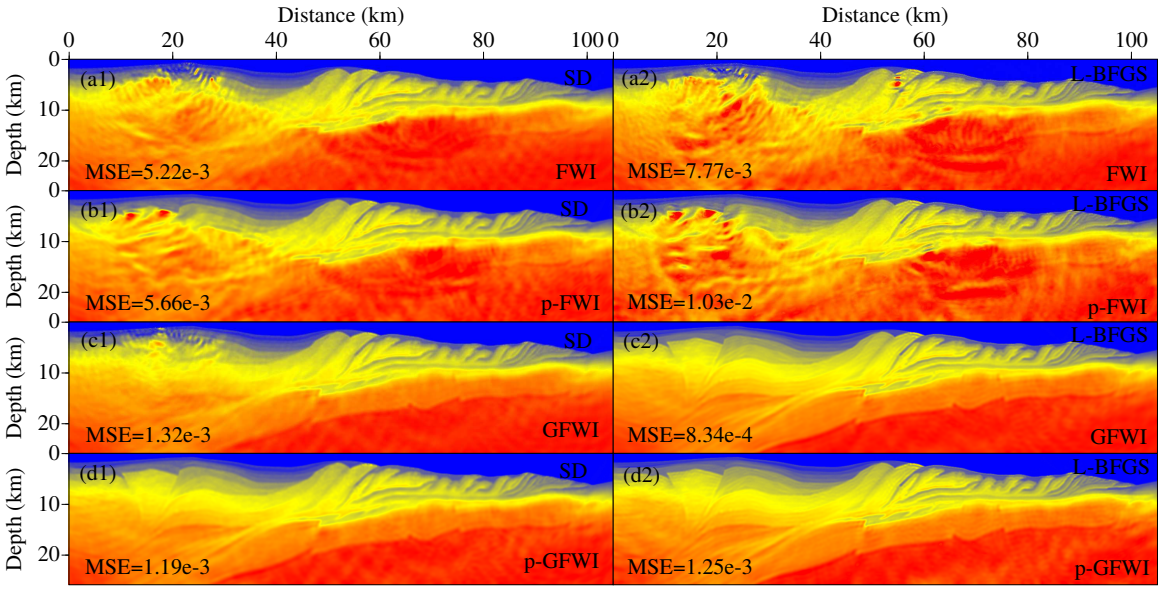

Figure 17: GO_3D_OBS model. Reconstructed models using (a1-d1) SD and (a2-d2) *l*-BFGS optimization methods. (a-b) FWI (a) without and (b) with pseudo-Hessian preconditioner (b). (c-d) GFWI (c) without and (d) with pseudo-Hessian preconditioner. MSE is shown in each panel.

artifacts above-described (Figures 17a1-b1 and a2-b2) that decrease the accuracy of the model in iterations (Figure 20b, gray and black symbols). Also, the shallow artifacts shown in the model inferred from SD GFWI impede the convergence (Figure 20a, blue circles), while SD p-GFWI achieves a reasonable convergence rate while generating quite accurate model (Figure 20, red circles). For this case study, *l*-BFGS p-GFWI provides the best convergence speed during the first multiscale step (Figure 20a, red triangles), while *l*-BFGS GFWI converges toward the best model during the two multiscale steps due to more stable deep velocity updates (Figure 20, blue triangles).

DISCUSSION

In this study, we present a generalized formulation of FWI, where we introduce the data-domain Hessian of the source problem involved in ES-FWI as a weighting of the FWI data misfit function. In this formulation, the original GN Hessian of FWI is decomposed into a source-side model-domain diagonal pseudo-Hessian associated with wavepaths connecting the sources to the scatterers and a receiver-side data-domain Hessian associated with wavepaths connecting the scatterers to the receivers. The pseudo-Hessian scales the amplitudes of the gradient with depth and its implementation doesn't generate computational overhead. The inverse data-domain Hessian performs a multidimensional deconvolution of the data residual source by source. This deconvolution requires the solution of a normal system for each source whose dimension is that of the receiver space. To mitigate this computational burden, we approximate the inverse data-domain Hessian with multi-dimensional nonstationary matching filters, which require a backward and a forward simulation per source. The combination of the source-side and receiver-side Hessians can be

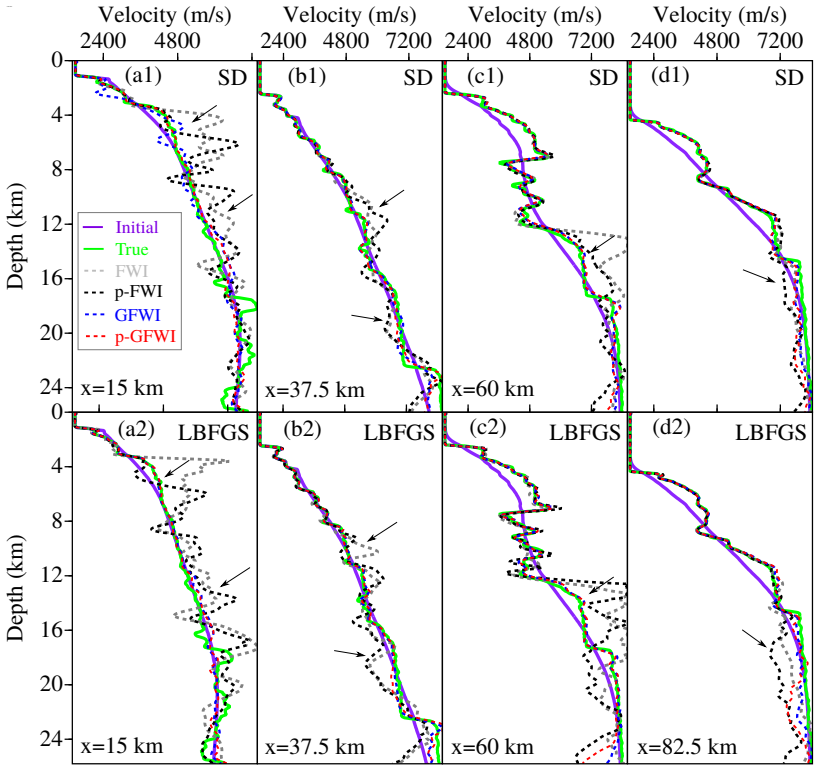

Figure 18: GO_3D_OBS model. Direct comparison of the true model (green), initial model (purple), reconstructed models using (a1-d1) SD and (a2-d2) l-BFGS optimization methods. (a-b) FWI without (gray) and with (black) pseudo-Hessian preconditioner. (c-d) GFWI without (blue) and with (red) pseudo-Hessian preconditioner. The arrows note the well reconstruction when decomposed GN Hessian is applied.

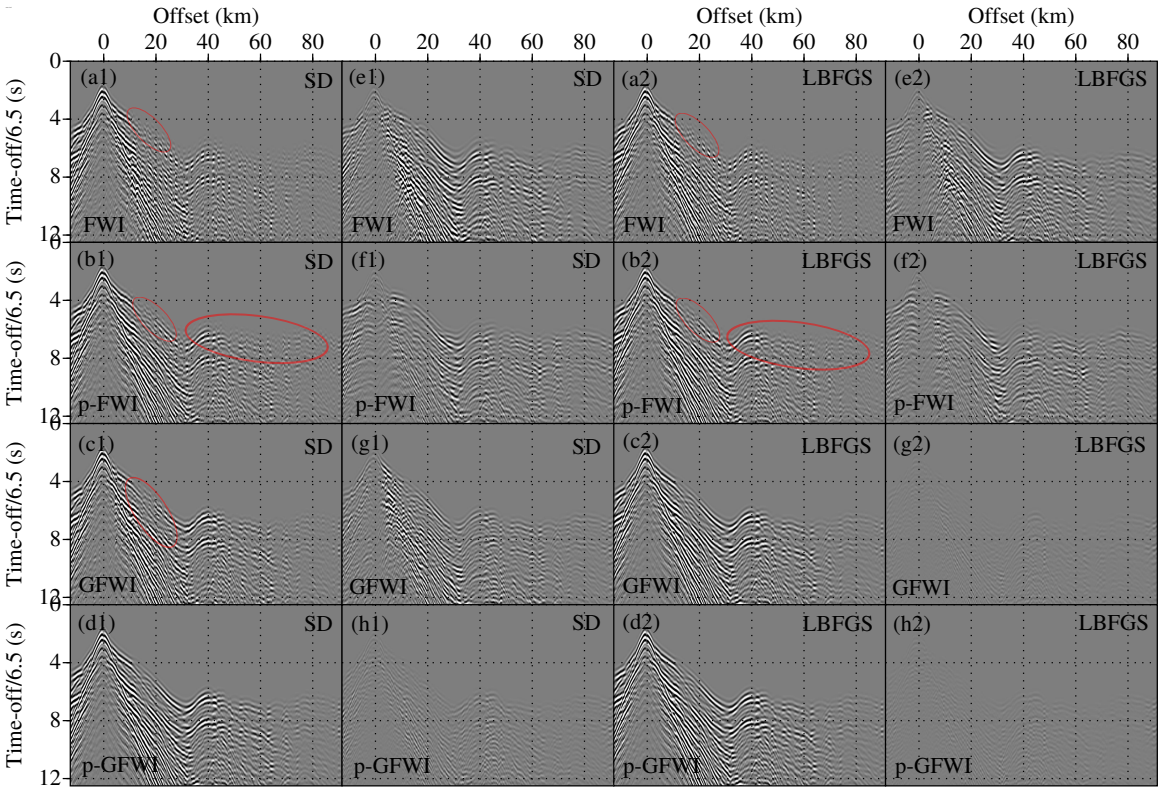

Figure 19: GO_3D_OBS model. Interleaved data (a-d) and data residuals (e-h) between observed data and simulated data in the final model with SD method (a1-h1) and *l*-BFGS method (a2-h2). (a-b) FWI (a) without and (b) with pseudo-Hessian preconditioner. (c-d) GFWI (c) without and (d) with pseudo-Hessian preconditioner. These interleaved data (a-d) could be compared with the interleaved data from the initial model shown in Figure 16b. The decrease of these data residuals (e-h) is compared with the initial data residuals in Figure 16c. The data mismatch is highlighted by red circles.

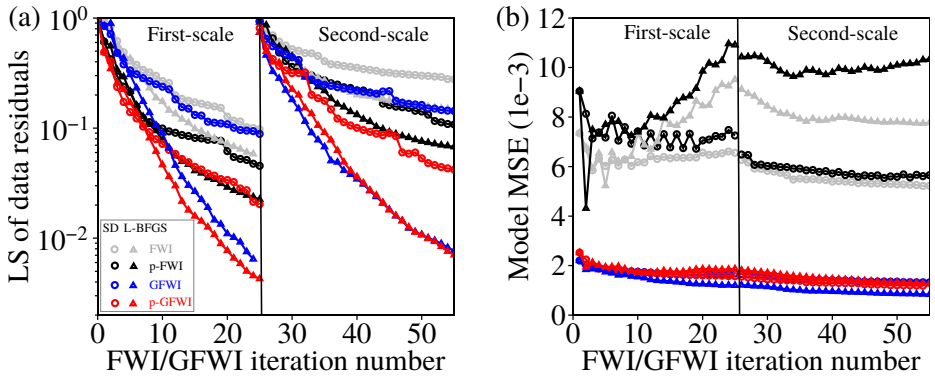

Figure 20: GO_3D_OBS model. (a) Convergence curves of normalized LS norm of data residuals using SD method (circles) and *l*-BFGS method (triangles). FWI without pseudo-Hessian preconditioner (gray) and with pseudo-Hessian preconditioner (black). GFWI without pseudo-Hessian preconditioner (blue) and pseudo-Hessian preconditioner (red). (b) Model MSE for FWI and GFWI using the same notation as in (a). Results are shown for the two multiscale steps [1.5; 1.8] Hz and [1.5; 4] Hz.

viewed as an alternative implementation of the all-at-once model-domain FWI GN Hessian where the partial derivative data describe wavepaths connecting the sources to the scatterers and the scatterers to the receivers. A key difference between the all-at-once GN Hessian implementation and the decomposed counterpart may be that the receiver-side Hessians are applied separately on each common-source data-residual gathers while the effects of these receiver-side Hessians are averaged over the full dataset in GN FWI. The numerical tests support that this decomposed GN Hessian not only accelerates the convergence of FWI but also mitigates the cycle-skipping issue.

The first main conclusion of the numerical experiments is that GFWI can be combined with l-BFGS to converge faster toward more accurate models. As such the two Hessians implemented in GFWI can be viewed as preconditioners of l-BFGS. This setting has provided the best results for the Marmousi benchmark while unpreconditioned l-BFGS provides more stable results for the complex GO_3D_OBS model. The second conclusion of the numerical experiments is that the GFWI formulation clearly contributes to mitigating some nonlinearities that can drive classical FWI toward spurious minima. To justify this property, it is worth recalling that GFWI is inspired by ES FWI. We have shown that the descent direction of alternating-direction ES-FWI and GFWI share the same Hessian decomposition. However, they differ in the incident wavefields: while the background wavefields are used in GFWI, ES-FWI relies on kinematically more accurate wavefields computed with the extended sources. The kinematic accuracy of the extended wavefields in ES-FWI is the leading ingredient in extending the search space of FWI and mitigating the cycle-skipping issue accordingly. However, the inverse data-domain Hessian can impact significantly upon the convergence of the inversion by weighting the data residuals as suggested by the current study. Operto et al. (2023) have shown that the inverse data-domain Hessian damps in offset the simulated component of the data residuals more aggressively than the recorded counterpart when the initial model is inaccurate. This results because the initial model is kinematically consistent with the simulated data and kinematically inconsistent with the recorded data. In this case, the multidimensional deconvolution performed by the inverse data-domain Hessian is more efficient when applied to the simulated data compared to the recorded data. Since this deconvolution tends to focus a diffraction hyperbola at its apex (amplitude weighting in offset), it decreases the contribution of the simulated data during the inversion at the benefice of the recoded counterpart. This is consistent with the fact that the convergence of ES-FWI is primarily driven by a measure of the misfocusing of the back-propagated recorded data in an inaccurate subsurface model rather than by a measure of the data fit. This misfocusing measure is the LS norm of the volume scattering source $\delta\mathbf{b}$, Appendix A, which should be zero if the background model is the true model. Figure 21 shows a recorded and simulated common-source gathers computed in the inaccurate S3 model (Marmousi benchmark) before and after multidimensional deconvolution by the inverse data-domain Hessian. The figure clearly shows the amplitude damping in offset in both the recorded data and the simulated data, this damping being more significant in the latter case consistently with the analysis of Operto et al. (2023, their figure 13). We also show the mean amplitude spectrum of the raw and deconvolved data residuals. The figure shows that the spectrum of the deconvolved data is pushed toward lower frequencies. This may be a second key factor that also contributes to make GFWI less sensitive to nonlinear effects. This frequency scaling may come from the expression of the FWI gradient when the forward problem is solved with a first-order velocity stress equation. In this case, a first derivative in time should be applied on the adjoint wavefield in the gradient. The

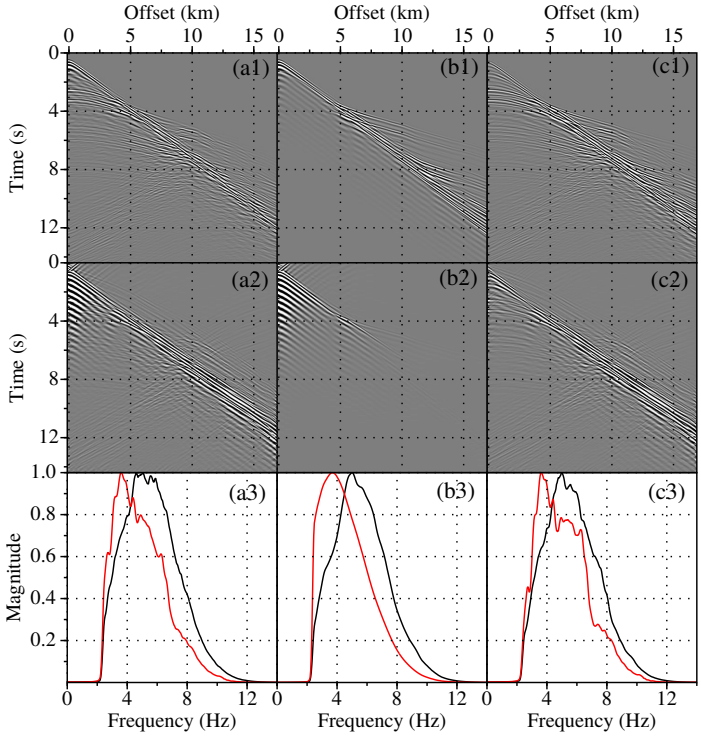

Figure 21: Marmousi II. Shot gather. (a1) True data. (b1) Simulated data in S3 initial model. (c1) Data residuals. (a2-c2) Deconvolved versions of (a-c) by inverse data-domain Hessian. (a3-c3) Normalized spectrum of (a1-c1) (black line) and (a2-c2) (red line).

inverse data domain Hessian may remove the effect of this temporal derivative by pushing the amplitude spectrum towards the low frequencies (see Sirgue and Pratt (2004, equation 16) for a discussion on the same line for the second-order wave equation). In Figure 21, the deconvolved data have been computed by solving the normal equation with 100 iterations of the Minimal residual Krylov method (MINRES). The figure 22 shows the deconvolved data obtained with the 2D Gabor-filter approximation. One can see that the matching filter provides a fairly good approximation of the deconvolved data inferred from MINRES. In particular, the frequency scaling above mentioned is fairly well reproduced.

The method may be improved with more accurate estimation of the inverse data-domain Hessian by performing multidimensional deconvolution with a preconditioned Krylov iterative solver as illustrated in Figure 21. This should contribute to further speeding up the convergence while reconstructing more accurate velocity models. The descent direction of Krylov iterative solver may be preconditioned by approximate inverse data-domain Hessian designed as the composition of a Laplace filter and a smooth scaling operator (Symes, 2008). The relevance of these ray-based approaches to precondition FWI problem involving both transmitted and reflected waves remains however an open issue (Métivier et al. (2015) for an attempt in this direction). Alternatively, a diagonal preconditioner inspired by the method of Rickett (2003), adapted in the data domain, may deserve investigations.

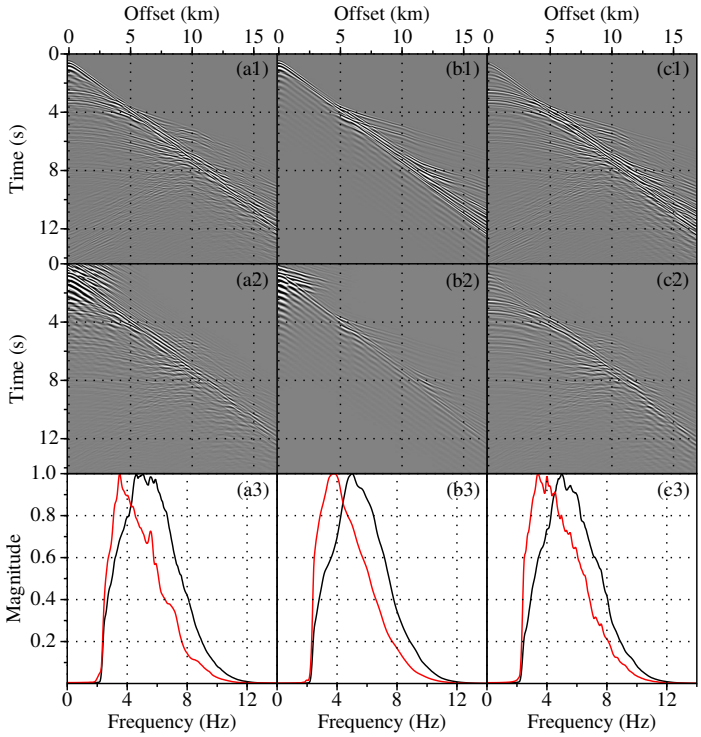

Figure 22: Marmousi II. Shot gather. (a1-c1) Observed data (a1), simulated data (b1) in S3 initial model and data residuals (c1). (a2-c2) Deconvolved versions of (a1-c1) by inverse data-domain Hessian estimated by matching filter. (a3-c3) Normalized spectrum of (a1-c1) (black line) and (a2-c2) (red line).

CONCLUSION

The application of GN Hessian is important for the fast convergence of FWI. In this study, we propose to split the GN Hessian into two parts by implementing the receiver-side component of the Hessian (the component of the partial derivative data describing the path connecting the scatterers to the receivers) as a data-domain weighting operator. It is recalled that this trick is inspired by the extended-source approach introduced in previous studies where the data-domain weighting operator is the inverse Hessian of the scattering source problem. The two parts of the split Hessian consist of a computationally free source-side diagonal pseudo-Hessian and receiver-side data-domain Hessian that is computed source by source. An efficient multi-dimensional non-stationary matching filter method is introduced to approximate the inverse data-domain Hessian. The two case studies presented here suggest that this split Hessian or only its receiver component can be used as a preconditioner of l-BFGS. In this framework, the proposed approach can be seen as a preconditioner to speed up the convergence of l-BFGS although the preconditioner generates some computational overhead at each iteration. The split GN iteration also can be used directly as an alternative to the GN iteration. We show that the split GN iteration can lead to more stable FWI results in the presence of moderate cycle skipping, probably due to the weighting applied directly by inverse data-domain Hessian on the data residuals in the gradient of the objective function. Future work aims to assess the effectiveness of split GN Hessian in multiparameter reconstruction and field data application.

APPENDIX A

ES-FWI IN A NUTSHELL

In this appendix, we review the GN iteration of ES-FWI when wavefields and parameters are updated in alternating mode to show that it leads to the GN Hessian decomposition that we use for FWI in this study, equation 14. The GN Hessian decomposition in ES-FWI results from the fact that the wavefields (via the scattering sources) are involved as optimization variables during a lower-level subproblem. The data-domain Hessians of the source problems are passed as apriori covariance operators to the upper-level $\mathbf{m}$-subproblem. This suggests that the data-domain Hessians of the source problem have already captured some effects of the GN Hessian of the $\mathbf{m}$-subproblem, hence leading to some simplifications of the latter.

ES-FWI extends the search space of FWI by computing wavefields that are more accurate than the background wavefields. More precisely, these extended wavefields should approximate as well as possible the true wavefields and match their restriction at receivers (the recorded data) accurately enough to avoid cycle skipping. To achieve this goal, let us first recall that, at a given FWI iteration k, the true wavefields $\mathbf{u}_s^*$ can be decomposed as the sum of the background wavefields $\mathbf{u}_s(\mathbf{m}^k)$ (used in classical FWI) and the scattered wavefield $\delta\mathbf{u}_s^*(\mathbf{m}^k)$ by the sought model perturbation $\delta\mathbf{m}^*(\mathbf{m}^k) = \mathbf{m}^* - \mathbf{m}^k$ where $\mathbf{m}^*$ denotes the true model (superscript $(\cdot)^*$ denotes true or measured quantities):

$$\mathbf{u}_s^* = \mathbf{u}_s(\mathbf{m}^k) + \delta\mathbf{u}_s^*(\mathbf{m}^k), \quad s = 1, ..., N_s \tag{A-1}$$

Accordingly, the true wavefields $\mathbf{u}_s^*$ are the solution of the following wave equation:

$$\mathbf{A}(\mathbf{m}^k)\mathbf{u}_s^* = \mathbf{b}_s^* + \delta\mathbf{b}_s^*, \tag{A-2}$$

where the wave equation operator $\mathbf{A}$ is built from the initial model $\mathbf{m}^k$, and the experimental sources $\mathbf{b}_s^*$ are augmented with the volume scattering sources $\delta\mathbf{b}_s^*(\mathbf{m}^k)$ of $\delta\mathbf{u}_s^*(\mathbf{m}^k)$, namely

$$\delta\mathbf{u}_s^* = \mathbf{A}^{-1}(\mathbf{m}^k)\delta\mathbf{b}_s^*. \tag{A-3}$$

The scattering sources $\delta\mathbf{b}_s^*$ are unknown as they depend on $\mathbf{u}_s^*$ and $\delta\mathbf{m}^*$ (Operto et al., 2023). However, we know the restriction of $\delta\mathbf{u}_s^*$ at receivers since they correspond to the data residuals $\delta\mathbf{d}_s^*$. Therefore, applying the observation operator $\mathbf{P}$ on both sides of equation A-3 gives

$$\delta\mathbf{d}_s^* = \mathbf{S}(\mathbf{m}^k)\delta\mathbf{b}_s^*, \tag{A-4}$$

where $\mathbf{S}_s(\mathbf{m}^k) = \mathbf{P}_s\mathbf{A}^{-1}(\mathbf{m}^k)$ is the forward modeling operator. The best we can do to estimate $\delta\mathbf{u}_s^*$ and hence approximate $\mathbf{u}_s^*$ is to estimate $\delta\mathbf{b}_s^*$ by solving the rank-deficient equation A-4 in a LS sense:

$$\min_{\delta\mathbf{b}_s} \|\mathbf{S}_s(\mathbf{m}^k)\delta\mathbf{b}_s - \delta\mathbf{d}_s^*(\mathbf{m}^k)\|_2^2 + \mu\|\delta\mathbf{b}_s\|_2^2, \tag{A-5}$$

where a damping regularization term has been introduced where μ is the penalty parameter. Since the source problem is underdetermined, we can always fit the scattered data accurately enough such that the recorded data and the simulated data in the extended space are not cycle skipped. The closed-form expression of the approximated scattering sources is given by:

$$\delta\mathbf{b}_s^e = \mathbf{S}_s(\mathbf{m}^k)^T\left(\mathbf{S}_s(\mathbf{m}^k)\mathbf{S}_s(\mathbf{m}^k)^T + \mu\mathbf{I}\right)^{-1}\delta\mathbf{d}_s^*(\mathbf{m}^k) = \mathbf{S}_s(\mathbf{m}^k)^T\mathbf{H}_s^d(\mathbf{m}^k)^{-1}\delta\mathbf{d}_s^*(\mathbf{m}^k), \tag{A-6}$$

where the subscript ^{e} stands for extended and the Hessian $\mathbf{H}_s^d(\mathbf{m}^k)$ is formulated in the data domain. The scattering sources are computed by propagating backward in time the weighted data residuals by the inverse data-domain Hessian. They represent the LS deconvolved form of the adjoint wavefields implemented in classical FWI. The extended wavefields follow by solving the wave equation with extended sources:

$$\mathbf{A}(\mathbf{m}^k)\mathbf{u}_s^e = \mathbf{b}_s^* + \delta\mathbf{b}_s^e. \tag{A-7}$$

To couple the extended wavefield reconstruction with parameter updating, the FWI data misfit function can be augmented with a source misfit function as

$$\min_{\mathbf{u},\mathbf{m}} \sum_s \|\mathbf{P}_s\mathbf{u}_s - \mathbf{d}_s^*\|_2^2 + \mu\sum_s \|\mathbf{A}(\mathbf{m})\mathbf{u}_s - \mathbf{b}_s^*\|_2^2, \tag{A-8}$$

where $\mathbf{d}_s^*$ denote the recorded data (van Leeuwen and Herrmann, 2013). We note that a change of variable $\mathbf{u}_s \rightarrow \delta\mathbf{b}_s$ allows us to obtain the misfit function given by equation A-5 after adding $\mathbf{m}$ in the optimization variables:

$$\min_{\delta\mathbf{b}_s,\mathbf{m}} \|\mathbf{S}_s(\mathbf{m})\delta\mathbf{b}_s - \delta\mathbf{d}_s^*(\mathbf{m})\|_2^2 + \mu\|\delta\mathbf{b}_s\|_2^2. \tag{A-9}$$

Therefore, we first solve the source subproblems A-9, whose solution is given in equation A-6, as a proxy to compute $\mathbf{u}_s^e$ by solving the wave equation A-7. This gives the same expression

for $\mathbf{u}_s^e$ as those that would be inferred by minimizing the misfit function A-8 because $\mathbf{u}_s^e$ and $\delta\mathbf{b}_s^e$ are related to an affine relationship involving the invertible operator $\mathbf{A}$ (Operto et al., 2023). Then, we update $\mathbf{m}$ by keeping $\mathbf{u}_s^e$ fixed in the frame of the alternating-direction approach. This amounts to minimizing the source misfit function, equation A-8, because $\mathbf{u}_s$ and $\mathbf{m}$ are processed as independent variables in the alternating-direction approach. To understand why minimizing $\delta\mathbf{b}_s$ pushes the updated model toward the true model, we may recall the two different formulations of the wave equation satisfied by the true wavefields:

$$\mathbf{A}(\mathbf{m})\mathbf{u}_s^* = \mathbf{b}_s^* + \delta\mathbf{b}_s^* \equiv \mathbf{A}(\mathbf{m}+\delta\mathbf{m}^*)\mathbf{u}_s^* = \mathbf{b}_s^* \tag{A-10}$$

Minimizing $\delta\mathbf{b}_s^*$ in the right-hand side of the left equation updates $\mathbf{m}$ in the wave-equation operator (left-hand side of the right equation) toward $\mathbf{m}^* = \mathbf{m} + \delta\mathbf{m}^*$.

The GN descent direction $\mathbf{p}^k$ for $\mathbf{m}$ is given by

$$\mathbf{p}^k = -\frac{\sum_s \mathbf{f}_s^e(\mathbf{m}^k)^T \left(\mathbf{S}_s(\mathbf{m}^k)^T \mathbf{H}_s^d(\mathbf{m}^k)^{-1} \delta\mathbf{d}_s^*(\mathbf{m}^k)\right)}{\sum_s \mathbf{f}_s^e(\mathbf{m}^k)^T \mathbf{f}_s^e(\mathbf{m}^k)}, \tag{A-11}$$

where $\mathbf{f}_s^e(\mathbf{m}^k) = \left(\partial\mathbf{A}(\mathbf{m}^k)/\partial\mathbf{m}\right)\mathbf{u}_s^e$ denotes the virtual sources in the extended space. This gives the descent direction highlighted by equation 1 where $W_{model} = \left(\mathbf{f}_s^e(\mathbf{m}^k)^T\mathbf{f}_s^e(\mathbf{m}^k)\right)^{-1}$ and $W_{data} = \left(\mathbf{S}_s(\mathbf{m}^k)\mathbf{S}_s(\mathbf{m}^k)^T + \mu\mathbf{I}\right)^{-1}$. Adapting this descent direction to classical FWI simply amounts to replacing $\mathbf{u}^e$ by $\mathbf{u}$ in the expression of the virtual sources $\mathbf{f}$ as shown by equation 14.

Finally, it has been shown by van Leeuwen (2019); Symes (2020); Gholami et al. (2022); Operto et al. (2023) that the bivariate minimization problem for $\mathbf{u}$ and $\mathbf{m}$, equation A-8, is equivalent to the generalized form of FWI given by

$$\phi^{g^e}(\mathbf{m}) = \sum_s \phi_s^{g^e}(\mathbf{m}) = \frac{1}{2}\sum_s \|\mathbf{P}_s\mathbf{u}_s(\mathbf{m}) - \mathbf{d}_s^*\|^2_{\mathbf{H}_s^d(\mathbf{m})^{-1}}, \tag{A-12}$$

The key difference between the misfit functions ϕ^g, equation 10, used in this study, and the ES-FW misfit function ϕ^{g^e}, equation A-12, is that the weighting operator depends on $\mathbf{m}$ in the extended space while it is computed in the starting model of the current iteration in the reduced space. The dependency on $\mathbf{m}$ modifies the kernel of the Born modeling operator by replacing the background wavefields with the extended wavefields hence leading to the search space extension. We remove this space extension in ϕ^g by removing the dependency of the weighting operator on $\mathbf{m}$.

REFERENCES

Aghamiry, H., A. Gholami, and S. Operto, 2019, Improving full-waveform inversion by wavefield reconstruction with alternating direction method of multipliers: Geophysics, **84(1)**, R139–R162.

Aghazade, K., A. Gholami, H. Aghamiry, and S. Operto, 2022, Anderson accelerated augmented Lagrangian for extended waveform inversion: Geophysics, **87**, no. 1, R79–R91.

Baeten, G., J. W. de Maag, R.-E. Plessix, R. Klaassen, T. Qureshi, M. Kleemeyer, F. ten Kroode, and Z. Rujie, 2013, The use of low frequencies in a full-waveform inversion and impedance inversion land seismic case study: Geophysical Prospecting, **61**, 701–711.

Beylkin, G., 1985, Imaging of discontinuities in the inverse scattering problem by inversion of a causal generalized Radon transform: Journal of Mathematical Physics, **26**, 99–108.

Brossier, R., S. Operto, and J. Virieux, 2009, Seismic imaging of complex onshore structures by 2D elastic frequency-domain full-waveform inversion: Geophysics, **74**, WCC105–WCC118.

Chauris, H. and E. Cocher, 2017, From migration to inversion velocity analysis: Geophysics, **82**, S207–S223.

Fu, L. and W. W. Symes, 2017, An adaptive multiscale algorithm for efficient extended waveform inversion: Geophysics, **82**, R183–R197.

Gao, L., Y. Pan, A. Rieder, T. Bohlen, and W. Mao, 2023, Multiparameter 2-d viscoelastic full-waveform inversion of rayleigh waves: a field experiment at krauthausen test site: Geophysical Journal International, **234**, 297–312.

Gholami, A., H. S. Aghamiry, and S. Operto, 2022, Extended full waveform inversion in the time domain by the augmented Lagrangian method: Geophysics, **87**, R63–R77.

Górszczyk, A. and S. Operto, 2021, GO_3D_OBS: the multi-parameter benchmark geomodel for seismic imaging method assessment and next-generation 3D survey design (version 1.0): Geoscientific Model Development, **14**, 1773–1799.

Guitton, A., 2004, Amplitude and kinematic corrections of migrated images for nonunitary imaging operators: Geophysics, **69**, 1017–1024.

Guo, G., S. Operto, A. Gholami, and H. S. Aghamiry, 2024, Time-domain extended-source full-waveform inversion: algorithm and practical workflow: Geophysics, **89**, R73–R94.

Hicks, G. J., 2002, Arbitrary source and receiver positioning in finite-difference schemes using Kaiser windowed sinc functions: Geophysics, **67**, 156–166.

Hou, J. and W. Symes, 2016, Approximate gauss-newton iteration for full-waveform inversion: Presented at the 2016 SEG International Exposition and Annual Meeting.

Hou, J. and W. W. Symes, 2015, An approximate inverse to the extended Born modeling operator: Geophysics, **80**, R331–R349.

———, 2017, An alternative formula for approximate extended born inversion: Geophysics, **82**, S1–S8.

Jin, S., R. Madariaga, J. Virieux, and G. Lambaré, 1992, Two-dimensional asymptotic iterative elastic inversion: Geophysical Journal International, **108**, 575–588.

Khalil, A., H. Hoeber, G. Roberts, and F. Perrone, 2016, An alternative to least-squares imaging using data-domain matching filters: 86th SEG Technical Program Expanded Abstracts 2016, 4188–4192.

Lambaré, G., S. Operto, P. Podvin, P. Thierry, and M. Noble, 2003, 3-D ray+Born migration/inversion - part 1: theory: Geophysics, **68**, 1348–1356.

Lambaré, G., J. Virieux, R. Madariaga, and S. Jin, 1992, Iterative asymptotic inversion in the acoustic approximation: Geophysics, **57**, 1138–1154.

Liu, Q., S. Beller, W. Lei, D. Peter, and J. Tromp, 2021, Pre-conditioned BFGS-based uncertainty quantification in elastic full-waveform inversion: Geophysical Journal International, **228**, 796–815.

Liu, Q., Y. Lu, S. Hui, and H. Zhang, 2019, Single-step data-domain least-squares reverse-time migration using Gabor deconvolution for subsalt imaging: IEEE Geoscience and Remote Sensing Letters, **17**, 13–16.

Liu, Q. and D. Peter, 2018, One-step data-domain least-squares reverse-time migration: Geophysics, **83**, R361–R368.

Liu, Y., W. Liu, Z. Wu, and J. Yang, 2022, Reverse time migration with an exact two-way illumination compensation: Geophysics, **87**, S53–S62.

Métivier, L. and R. Brossier, 2016, The SEISCOPE optimization toolbox: A large-scale nonlinear optimization library based on reverse communication: Geophysics, **81**, F11–

F25.

Métivier, L., R. Brossier, A. Hoffmann, J.-M. Mirebeau, G. Provenzano, A. Tarayoun, and P. Yong, 2024, Coherence-enhancing anisotropic diffusion filter for 3d high-resolution reconstruction of p-wave velocity and density using full-waveform inversion: Application to a north sea ocean bottom cable data set: GEOPHYSICS, **89**, R33–R58.

Métivier, L., R. Brossier, and J. Virieux, 2015, Combining asymptotic linearized inversion and full waveform inversion: Geophysical Journal International, **201**, 1682–1703.

Métivier, L., R. Brossier, J. Virieux, and S. Operto, 2013, Full Waveform Inversion and the truncated Newton method: SIAM Journal On Scientific Computing, **35(2)**, B401–B437.

Nocedal, J., 1980, Updating Quasi-Newton Matrices With Limited Storage: Mathematics of Computation, **35**, 773–782.

Nocedal, J. and S. J. Wright, 2006, Numerical optimization: Springer, 2nd edition.

Operto, S., R. Brossier, Y. Gholami, L. Métivier, V. Prieux, A. Ribodetti, and J. Virieux, 2013, A guided tour of multiparameter full waveform inversion for multicomponent data: from theory to practice: The Leading Edge, **Special section Full Waveform Inversion**, 1040–1054.

Operto, S., A. Gholami, H. S. Aghamiry, G. Guo, , S. Beller, K. Aghazade, F. Mamfoumbi, L. Combe, and A. Ribodetti, 2023, Extending the search space of FWI beyond the single-scattering born approximation: Geophysics, **88(6)**, R671–R702.

Operto, S., A. Miniussi, R. Brossier, L. Combe, L. Métivier, V. Monteiller, A. Ribodetti, and J. Virieux, 2015, Efficient 3-D frequency-domain mono-parameter full-waveform inversion of ocean-bottom cable data: application to Valhall in the visco-acoustic vertical transverse isotropic approximation: Geophysical Journal International, **202**, 1362–1391.

Operto, S., J. Virieux, J. X. Dessa, and G. Pascal, 2006, Crustal imaging from multifold ocean bottom seismometers data by frequency-domain full-waveform tomography: application to the eastern Nankai trough: Journal of Geophysical Research, **111**, doi:10.1029/2005JB003835.

Pan, W., K. A. Innanen, and W. Liao, 2017, Accelerating hessian-free gauss-newton full-waveform inversion via l-bfgs preconditioned conjugate-gradient algorithm: Geophysics, **82**, R49–R64.

Pan, W., K. A. Innanen, G. F. Margrave, M. C. Fehler, X. Fang, and J. Li, 2016, Estimation of elastic constants for HTI media using Gauss-Newton and full-Newton multiparameter full-waveform inversion: Geophysics, **81**, R275–R291.

Plessix, R. E., 2006, A review of the adjoint-state method for computing the gradient of a functional with geophysical applications: Geophysical Journal International, **167**, 495–503.

Plessix, R. E. and C. Perkins, 2010, Full waveform inversion of a deep water ocean bottom seismometer dataset: First Break, **28**, 71–78.

Pratt, R. G., C. Shin, and G. J. Hicks, 1998, Gauss-Newton and full Newton methods in frequency-space seismic waveform inversion: Geophysical Journal International, **133**, 341–362.

Ravaut, C., S. Operto, L. Improta, J. Virieux, A. Herrero, and P. dell'Aversana, 2004, Multi-scale imaging of complex structures from multi-fold wide-aperture seismic data by frequency-domain full-wavefield inversions: application to a thrust belt: Geophysical Journal International, **159**, 1032–1056.

Rickett, J. E., 2003, Illumination-based normalization for wave-equation depth migration: Geophysics, **68**, 1371–1379.

Shin, C., S. Jang, and D. J. Min, 2001, Improved amplitude preservation for prestack depth

migration by inverse scattering theory: Geophysical Prospecting, **49**, 592–606.

Sirgue, L., O. I. Barkved, J. Dellinger, J. Etgen, U. Albertin, and J. H. Kommedal, 2010, Full waveform inversion: the next leap forward in imaging at Valhall: First Break, **28**, 65–70.

Sirgue, L. and R. G. Pratt, 2004, Efficient waveform inversion and imaging : a strategy for selecting temporal frequencies: Geophysics, **69**, 231–248.

Symes, W. W., 2008, Approximate linearized inversion by optimal scaling of prestack depth migration: Geophysics, **73**, R23–R35.

———, 2020, Wavefield reconstruction inversion: an example: Inverse Problems, **36**, 105010.

Tang, Y. and S. Lee, 2010, Preconditioning full waveform inversion with phase-encoded hessian: SEG International Exposition and Annual Meeting, SEG–2010.

ten Kroode, F., 2012, A wave-equation-based kirchhoff operator: Inverse Problems, **28**, 115013.

Thierry, P., G. Lambaré, P. Podvin, and M. Noble, 1999a, 3-D preserved amplitude prestack depth migration on a workstation: Geophysics, **64**, 222–229.

Thierry, P., S. Operto, and G. Lambaré, 1999b, Fast 2D ray-Born inversion/migration in complex media: Geophysics, **64**, 162–181.

van Leeuwen, T., 2019, A note on extended full waveform inversion: arXiv preprint arXiv:1904.00363.

van Leeuwen, T. and F. Herrmann, 2016, A penalty method for PDE-constrained optimization in inverse problems: Inverse Problems, **32(1)**, 1–26.

van Leeuwen, T. and F. J. Herrmann, 2013, Mitigating local minima in full-waveform inversion by expanding the search space: Geophysical Journal International, **195(1)**, 661–667.

Virieux, J., 1984, SH wave propagation in heterogeneous media: Velocity-stress finite difference method: Geophysics, **49**, 1259–1266.

Warner, M., A. Ratcliffe, T. Nangoo, J. Morgan, A. Umpleby, N. Shah, V. Vinje, I. Stekl, L. Guasch, C. Win, G. Conroy, and A. Bertrand, 2013, Anisotropic 3D full-waveform inversion: Geophysics, **78**, R59–R80.

Yang, P., R. Brossier, L. Métivier, J. Virieux, and W. Zhou, 2018, A Time-Domain Preconditioned Truncated Newton Approach to Multiparameter Visco-acoustic Full Waveform Inversion: SIAM Journal on Scientific Computing, **40**, B1101–B1130.

Yang, Y., 2021, Anderson acceleration for seismic inversion: Geophysics, **86**, R99–R108.

Yong, P., R. Brossier, and L. Métivier, 2022, Parsimonious truncated Newton method for time-domain full waveform inversion based on Fourier-domain full-scattered field approximation: Geophysics, **87**, R123–R146.